



# Statistical damage theory of 2D lattices: Energetics and physical foundations of damage parameter

A. Rinaldi <sup>a,\*</sup>, Y.-C. Lai <sup>b</sup>

<sup>a</sup> *Materials Science and Technology, Department of Chemical Science and Technology, University of Rome  
“Tor Vergata”, Via della Ricerca Scientifica, 00133 Roma, Italy*

<sup>b</sup> *Electrical Engineering, Arizona State University, Tempe, AZ 85287, United States*

Received 12 November 2006; received in final revised form 4 January 2007

Available online 15 March 2007

---

## Abstract

The paper presents an in-depth analysis of two-dimensional disordered lattices of statistical damage mechanics for the study of quasi-brittle materials. The strain energy variation in correspondence to damage formation is thoroughly examined and all the different contributions to the net energy changes are identified and analyzed separately. We demonstrate that the introduction of a new defect in the microstructure produces a perturbation of the microscopic random fields according to a principle of maximum energy dissipation. A redistribution parameter  $\eta$  is introduced to measure the load redistribution capability of the microstructure. This parameter can be estimated from simulation data of detailed models. This energetic framework sets the stage for the investigation of the statistical foundations of the damage parameter as well as the damage localization. Logical statistical arguments are developed to derive two analytical models (a maximum field model and a mean field one) for the estimate of the damage parameter via a bottom-up approach that relates the applied load to the microstructural disorder. Simulation data provided input to the statistical models as well as the means of validation. Simulated tensile tests of honeycomb lattices with mechanical disorder demonstrate that long-range interactions amongst sets of microcracks with different orientations play a fundamental role already in damage nucleation as well as in the homogeneous–heterogeneous transition. A functional “hierarchy of sets” of grain boundaries, based on their orientation in relation to the applied load, seems to emerge from this study. Results put in evidence the ability of discrete models of capturing seamlessly the damage anisotropy. The ideas exposed inhere should be useful to develop a full

---

\* Corresponding author. Tel.: +39 349 6778202; fax: +39 0672594328.  
E-mail address: [antonio.rinaldi@gmail.com](mailto:antonio.rinaldi@gmail.com) (A. Rinaldi).

rational model for disordered lattices and, later, to extend the approach to discrete models with solid elements. The findings suggest that statistical damage mechanics might aid in the quest of reliable and physically sound constitutive relations of damage, even in synergy with micromechanics.

© 2007 Elsevier Ltd. All rights reserved.

*Keywords:* Lattice models; Microstructure; Non-local effects; Damage parameter; Statistical damage

---

## 1. Introduction

Engineering materials normally experience a progressive deterioration of their mechanical and functional properties under the action of applied load and external stimuli, both during the manufacturing process and in the working environment. On the microscale this damaging process is the irreversible transformation of the microstructure via nucleation, propagation and coalescence of defects, such as microcracks and voids. Several continuum damage models have flourished in the years for ductile and brittle materials. Elasto-plastic and visco-plastic models were proposed, for example, by Simo and Ju (1987), Hansen and Schreyer (1994), Lubarda and Krajcinovic (1995), Cannmo et al. (1995), Sazuk et al. (2003), Brünig (2004), Voyiadjis et al. (2004), Bonora et al. (2005), Pierard and Doghri (2006). Other examples related to brittle solids are found in Budiansky and O’Connell (1976), Krajcinovic and Fonseka (1981a,b), Chaboche (1988a,b). Overviews of continuum damage modeling with extensive references are offered, for example, by Lemaitre (1996), Krajcinovic (1996) and Voyiadjis and Kattan (1999). The damage state is typically described by a damage parameter chosen on a phenomenological base or derived with micromechanics and homogenization techniques. Damage is intrinsically a multiscale problem where one or few micro defects in a localized region have a strong influence on the macroscale response of the solid. The presence of two length scales is an intrinsic difficulty for continuum damage modeling, more suited to capture macroscopic effects. Although “integrated” approaches exist, where coupled governing equations for microscale and macroscale are solved at once, such as the multifield theories in Mariano and Stazi (2001), the multiscale problem is often approached with a modular strategy, where separate models for the two scales are properly linked together. This approach favors the implementation of damage models within commercial finite element software. “Length scale” parameters are used in non-local continuum to transfer the microscopic changes within the microstructure to the macroscale but such phenomenological parameters are difficult to justify by a physical standpoint. The representative volume element (RVE) is typically used in micromechanics for the same purpose. However, the effective properties of an RVE depend on the averaging technique used for the global redistribution of local effects due to individual microcracks. The “dilute concentration” and self-consistent models in Krajcinovic (1996) are emblematic examples in this respect. Micromechanical models are usually adequate in the range of small damage density, as long as the damage distribution is statistical homogeneous.

The abundance of scalar, vectorial and tensorial damage parameters found in the referenced work expresses the fact that the measure of damage is not only specific to the number, shape and size of microdefects but to the underlying damage mechanism as well. Scalar damage parameters are used to model isotropic damage, e.g. Lemaitre (1985a,b), Krajcinovic and Fonseka (1981a,b) or Tvergaard (1990). The experiments by Hayhurst (1972),

Chow and Wang (1987) and Audoin and Baste (1994), amongst others, demonstrated the anisotropic nature of damage even in materials that are isotropic in pristine state. Chow and Wang put in evidence that isotropic damage models tend to underestimate the effect of damage in comparison to anisotropic damage and that the nature of damage is strongly dependent on the loading path close to failure. Therefore, damage-induced anisotropy needs to be included in the damage analysis to yield robust and reliable results. More recently Litewka and Debinski (2003) modeled rock-like materials with an isotropic model in pristine conditions and discussed the elastic anisotropy induced by damage. The load applied to brittle rock causes, in fact, the formation of oriented microcracks orthogonal to the direction of max principal stress. Cordebois and Sidorff (1979), Betten (1983), Krajcinovic (1983), Horii and Nemat-Nasser (1983), Chow and Wang (1987), Chaboche (1988a,b), Murakami (1988), Ju (1990), Voyiadjis et al. (2004) and Brünig (2004), amongst others, used second and higher order tensors to model anisotropic damage.

Besides the mainstream of continuum damage mechanics, an alternative theoretical framework, focused on discrete modeling techniques and generally referred to as statistical damage mechanics, has been developed by several researchers, e.g. Hansen et al. (1989), Curtin and Scher (1990), Krajcinovic and Basista (1991), Jagota and Bennison (1995), Krajcinovic and Vujosevic (1998), Delaplace et al. (1996), Mastilovic and Krajcinovic (1999), Sahimi (2000), Rinaldi et al. (2006a). These models tend to be well suited for multiscale problems because they can incorporate several microstructural features into the model by using statistical information that can be measured directly and, without making further assumptions, are capable of scaling the material response to the macrolevel. Discrete models have been mostly used to explore qualitative aspects of the damage process in quasi-brittle materials and, unlike micromechanical models, have the advantage of being seamlessly applicable also when the microstructure is not statistically homogeneous. The drawback is the computational cost that limits the model size. Although, analytical statistical models were developed for the one-dimensional case, e.g. in Krajcinovic (1996), two and tri-dimensional models, requiring numerical solution, are necessary to capture the defects interaction in real materials and reproduce the non-local effect caused by damage. For this reason, considerable attention has been drawn by lattice models, which provide simple representations of complex systems, such as the disordered microstructures of ceramics, concrete and other quasi-brittle polycrystalline materials. Contrarily to a classical continuum scheme, lattice models can resolve individual grain boundaries and are convenient for the study of brittle damage by intergranular cracking. Experimental work by Christopher et al. (2003) pointed out that grain boundaries take part in different degrees to the damage propagation based on their orientations with respect to the applied load. This dependence, intimately related to the damage-induced anisotropy, will be outlined by the results presented here.

Novel results in discrete damage modeling were discussed by Krajcinovic and Rinaldi (2005) and Rinaldi et al. (2006a,b, 2007); about the uniaxial response of a two-dimensional lattices made of spring elements. Therein, the authors propose a phenomenological constitutive model based on simulation data on disordered lattice structures of different size. Their model describes well the macroscopic behavior from simulations but the connection between the damage parameter and the microstructural evolution is still unclear. They examined the hardening–softening transition in brittle materials that affects brittle solid at the onset of the damage localization preludes the structural failure as reported, for example by Hegemier and Read (1985). This paper pertains the same lattice models and is virtually the prosecution of the referenced work. After a brief overview of the results

by Krajcinovic and Rinaldi (2005), Rinaldi et al. (2006a) to make the connection, new results will be presented in two parts. The first part of the paper addresses energetic aspects and establishes the variational formulation of the selected spring network. In particular we show that the perturbation microfield<sup>1</sup> obeys a principle of maximum dissipation of potential energy. The second part presents a bottom-up modeling technique, capable of rendering the macroscopic damage parameter based on a rigorous statistical treatment of several microparameters and on some ideas developed in the energetic section. The driving argument throughout the paper is the role that the elastic perturbation, induced in the microstructure by the existing microcracks, has on the anisotropic evolution of damage and on the homogeneous–heterogeneous phase transition prior to failure. The far reaching objective is to gain a better understanding of the physics underlying the homogeneous–heterogeneous phase transition occurring at the peak of the force response of brittle solids and to expose few fundamental ideas useful to formulate “mechanistic” type of constitutive relations for lattice models. Such physically-based models are not yet available although very desirable. Therefore, the emphasis is on the creation of a rational model for spring lattices. The constitutive models derived analytically will be checked against the output data from the simulations that they aim to capture. Previous work in literature demonstrated that lattice models can be calibrated against real experiments and that simulations can be regarded as numerical experiments suitable for validation purposes. Van Mier et al. (2002), for example, showed the agreement between simulated tensile tests and actual tests for concrete using lattice models of the microstructure similar to ours. Also, the theory of elastic networks has been applied for decades already, e.g. Hrennikoff (1941), yielding reliable representations of real systems, such as spring, truss and frame structures. Usage of these models in structural design is a proved and consolidated practice in the field of civil and mechanical engineering that does not need any further validation as far as our simulations are concerned. Spring networks are also instrumental in the developing phase of our approach, before the eventual extensions of the principles illustrated inhere to models of 2D and 3D microstructures with solid elements.

## 2. Background: previous results

Two-dimensional spring networks offer simplistic representations of random polycrystalline microstructures. Fig. 1 shows an instance of a lattice with perfect geometry for  $N = 12$ , with  $N$  being the number of grains on each side. The proper constraints used by Krajcinovic, Rinaldi and coworkers for the simulations of tensile test in the  $x$ -direction are displayed as well. Each grain of the polycrystalline material maps into a lattice node, while each link marks a grain boundary and transmit the cohesive normal force between adjacent grains. To reproduce the intergranular cracking process of brittle materials, the links behave as decohesive elements and are linear springs of equal stiffness that breaks under tensile load when a strain threshold (or the corresponding strength) is reached. The disorder, necessary for any localization process, is quenched in the lattice both by using a random Delaunay triangular network (geometric disorder) and by sampling the failure strains from a uniform distribution starting at zero (mechanical disorder). Being the critical strains independent of the spring length, the two options are decoupled and

---

<sup>1</sup> Microfield in the paper means field extended to the lattice domain.

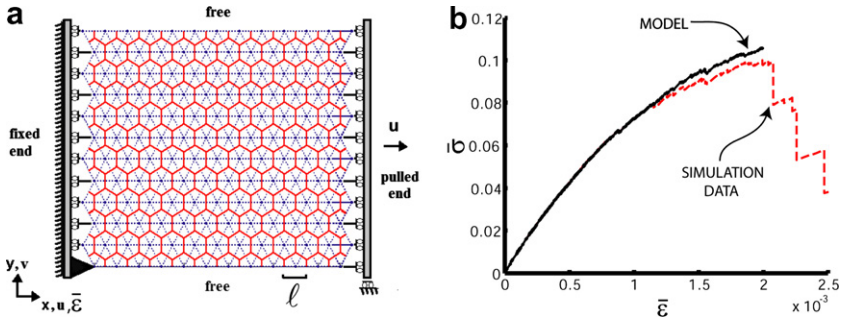


Fig. 1. Disordered lattice with perfect geometry ( $N = 12$ ) and comparison between simulation data (dashed) vs. predicted response (solid) from (1) and (2) in hardening phase for  $N = 48$ . The agreement is very good at small damage density.

can be managed independently. No initial damage distribution is assumed in pristine state. Limited to the case of static uniform tensile loading, the macro stress–strain response of a damaged lattice of size  $L$  is generally expressed by the scalar relation

$$\bar{\sigma}(\bar{\varepsilon}, L) = \bar{K}_0 [1 - \bar{D}(\bar{\varepsilon}, L)] \bar{\varepsilon}. \tag{1}$$

In the referenced work, the authors considered lattice sizes  $N = [24, 48, 72, 96, 120, 192, 288]$  and identified suitable definitions for the damage parameter  $\bar{D}(\bar{\varepsilon}, L)$  in the hardening phase (i.e.  $\partial \bar{\sigma} > 0, \bar{\varepsilon} < \bar{\varepsilon}_{\text{peak}}$ ) of the stress–strain response, namely:

$$\bar{D}(\bar{\varepsilon}, L) = \frac{n(\bar{\varepsilon}, L)}{\alpha_1 L^2} \quad (\bar{\varepsilon} \leq \bar{\varepsilon}_{\text{peak}}), \tag{2}$$

where  $n(\bar{\varepsilon}, L)$  are the broken bonds at the given  $\bar{\varepsilon}$  and  $\alpha_1 = 0.4$  is the numerical estimate from simulations. The bar sign over the symbols indicate effective quantities measured on the macroscale. The derivation of definitions (2) was partly empirical and partly theoretical. The transition happening at  $\bar{\varepsilon}_{\text{peak}}$  from damage nucleation in the hardening phase and damage propagation in the softening phase provided the physical reference around which phenomenological observations, fractal analysis and finite-scale data transformations were logically combined. The analytical expression for the mean value of  $n$  was

$$n(\bar{\varepsilon}, L) = \alpha_1 L^2 \left[ a_1 \bar{\varepsilon} + b_1 \frac{\bar{\varepsilon}^2}{L^{z_1}} \right]. \tag{3}$$

The validation of this theory was done by verifying the good agreement between simulation data and Eq. (1) (Rinaldi et al., 2006a). The parameters are reportedly  $\{a_1, b_1, z_1\} = \{275, -14, 862, -0.035\}$ . This set of results provides a promising instance of “bridging the scales” in the field of strength of materials and damage mechanics. The scaling relations (2) and (3) means that knowledge of  $n$  and  $\Delta n$  on one scale implies such knowledge on any scale and that model (1) would hold for lattices of any size, which tends to be confirmed by the good agreement with simulation data. In this paper, the focus moves from the size effects onto energetic and statistical foundations of definition (2) for  $\bar{D}$  in the hardening phase. New simulations have been carried out to these purposes.

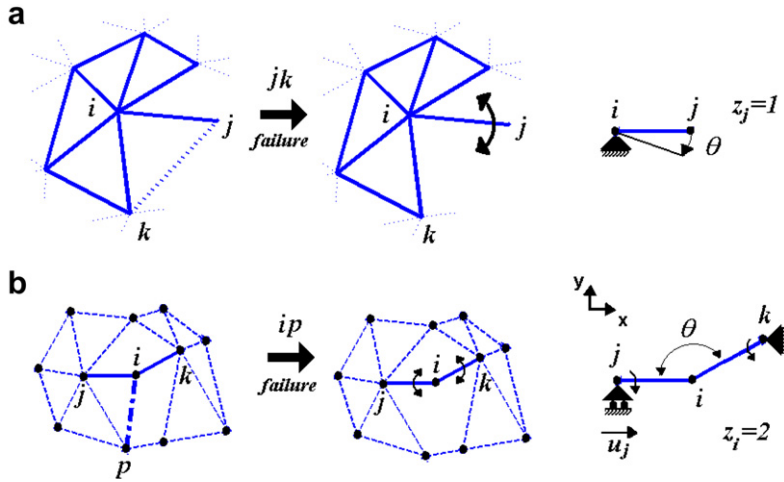


Fig. 2. Formation of dandling link from rupture of the  $ij$ th link (a) and of kinematical mechanism from rupture of  $ip$ th link (b) in the primary lattice.

### 3. Simulations: technique and data

Standard finite elements analysis (FE) have been implemented purposely for simulat- ing tensile tests in a damage-controlled mode and generate information for the study of the transition and the detection of avalanches. The general structure of the static linear elastic FE problem is described by the matrix equation  $\mathbf{K}_L \mathbf{u}_L = \mathbf{F}_L$ , where  $\mathbf{K}_L$  is the sys- tem stiffness matrix of the lattice and  $\{\mathbf{F}_L, \mathbf{u}_L\}$  are the nodal vectors of the external forces and displacements associated to the grains (the nodes). For a discrete structure like the lattice, the matrix  $\mathbf{K}_L$  is obtained by the standard “assembly” procedure when both the orientation  $\vartheta_{(ij)}$  and the scalar stiffness  $k_{(ij)}$  of the  $ij$ th spring<sup>2</sup> connecting the  $i$ th and  $j$ th nodes are known for all the  $Q$  “active” elements, where active refers to “pristine” or “broken but compressed” springs. It is known that the global representa- tion of the stiffness matrix of a spring element has four degrees of freedom (*dof*).  $\mathbf{K}_L$  is assembled by summing the augmented matrices  $\hat{\mathbf{K}}_{(ij)}^{EL}$  of the  $Q$  active links, i.e.  $\mathbf{K}_L = \sum_q^Q \hat{\mathbf{K}}_q^{EL}$ . The ensemble of active links changes with the damage process and  $\mathbf{K}_L$  must be updated at every damage step, when a new spring breaks or a broken one closes, becoming active again. Close to localization, the selected lattice suffers the forma- tion of dandling springs and local mechanisms (Fig. 2), which cause local instabil- ities and render  $\mathbf{K}_L$  singular even after the application of the boundary conditions. The  $ij$ -link in Fig. 2a becomes dandling when the coordination number  $z_j$  of the  $j$ th node drops to  $z_j = 1$  after the rupture of the  $kj$ -link. Instead, a kinematical mechanism with 1 degree of freedom forms locally if  $z_i = 2$  and the  $ij$ th and  $ik$ th survivor springs of the

<sup>2</sup> In the discussion a generic spring element can be referred to both as  $ij$ th link, if the focus is on the end nodes  $i$  and  $j$ , or as  $p$ th link, if the focus is on the list of links (e.g. for sums over a list of elements). Hence double notation,  $\varepsilon_{(ij)}$  and  $\varepsilon_p$ , is used depending on the circumstances. In the former case parentheses are used for the subscripts to avoid confusion with the index notation  $\varepsilon_{ij}$  customarily reserved in solid mechanics for second order tensors.

$i$ th node are non-consecutive (non-adjacent in the Voronoi graph), as depicted in Fig. 2b when the  $ip$ -link breaks. A “stability check” was implemented to detect and remove these local instabilities by excluding the unstable links from the assembly procedure, which increased significantly the duration of the simulation.

Damage-controlled simulations are achieved by searching the critical macroconfigurations that determines the failure of the unbroken link with highest damage affinity  $\mathcal{A}_{(ij)} = (1/2)k_{(ij)}\ell_{(ij)}(\varepsilon_{(ij)}^2 - \varepsilon_{(ij)}^{*2})$ , where  $\varepsilon_{(ij)}$  and  $\varepsilon_{(ij)}^*$  are the current strain and the critical tensile strain of the  $ij$ th link respectively and  $\{k_{(ij)}, \ell_{(ij)}\}$  are the stiffness and initial length. By letting  $\bar{u}$  be an arbitrary macrodisplacement imparted to the lattice, a trial displaced configuration is computed in a displacement-controlled fashion, with  $u_{(ij)}$  and  $\varepsilon_{(ij)}$  being the trial elongation and strain of the generic  $ij$ th link on the microscale. Since  $\varepsilon_{(ij)} \propto \bar{u}$  in the linear elastic framework, the next spring to fail as  $\bar{u}$  increases is the one with the highest ratio  $\lambda_{(ij)} = \varepsilon_{(ij)}/\varepsilon_{(ij)}^*$  between actual strain and critical strain from the quenched distribution, because it reaches first the failure condition  $\lambda_{(ij)} = 1$  (i.e.  $\mathcal{A}_{(ij)} = 0$ ). Then, the corresponding lattice displacement  $\bar{u}^*$ , computed from the trial  $\bar{u}$ , is  $\bar{u}^* = \bar{u}/\lambda_{(ij)}^{\text{MAX}}$ . As a second step,  $\mathbf{K}_L$  is updated by removing from the active set the  $p$ th link with  $\lambda_p = \lambda_{(ij)}^{\text{MAX}}$  and the new lattice configuration at  $\bar{u}^*$  is computed, which allows assessing the load drop associated to new damage. This two-step procedure is repeated until the lattice breaks down. A similar approach was used by Delaplace et al. (1996) for fuse lattices. Data  $\{\bar{F}, \bar{u}\}$  are collected only in correspondence to the critical macrodisplacements  $\bar{u}^*$  where new damage forms. The corresponding engineering  $\bar{\sigma}$ – $\bar{\varepsilon}$  curve is obtained from  $\bar{\sigma} = \bar{F}/L$  and  $\bar{\varepsilon} = \bar{u}/L$ . The displacement-controlled curve, typically observed in real monotonic tensile tests, is obtained from the envelope of the damage control response with the constraint that  $\Delta\bar{u} \geq 0$  always.

The tensile tests in this paper are simulated on disordered lattices with random mechanical properties, analogously to Krajcinovic and Rinaldi (2005), but with perfect geometry, as in Hansen et al. (1989) and Fig. 1a. In Section 5 we analyze four random replicates of such lattice for  $N = \{24, 48, 96, 192\}$  and explain the motivations for choosing a perfect geometry. New simulation data (full line) for  $N = 48$  plotted in Fig. 1b matches the average response (asterisk line) estimated from Eqs. (1)–(3) in the hardening phase. This result is expected since the honeycomb lattice is just a special realization of the distorted lattice by Krajcinovic and Rinaldi and their constitutive model should hold. Representative simulation data are shown in Fig. 3 for the  $48 \times 48$  honeycomb lattice. The displacement-controlled response (bold full line) enveloping the damage-controlled response (thin dotted line) are visible in plot A. The evolution of the total ruptures  $n$  and of the secant stiffness  $\bar{K} = \bar{\sigma}/\bar{\varepsilon}$  are shown in plots B and D. The meaning of plot C about strain energy dissipation will be clarified in the next section.

#### 4. Energetics of the lattice in uniaxial test

This section analyzes the energetic formulation of the lattice problem. The force response is a serrated saw-toothed diagram as in Fig. 4a, where abrupt stiffness drops separating linear elastic regions relate to the ongoing damage process. The spring-elongation microfield  $u_{(ij)}$  and the nodal displacement vector  $\mathbf{u}_L$  correspond to the imposed  $\bar{u}$  at state P. For the tensile test the strain energy  $U$  stored in the lattice can be expressed in three equivalent forms as

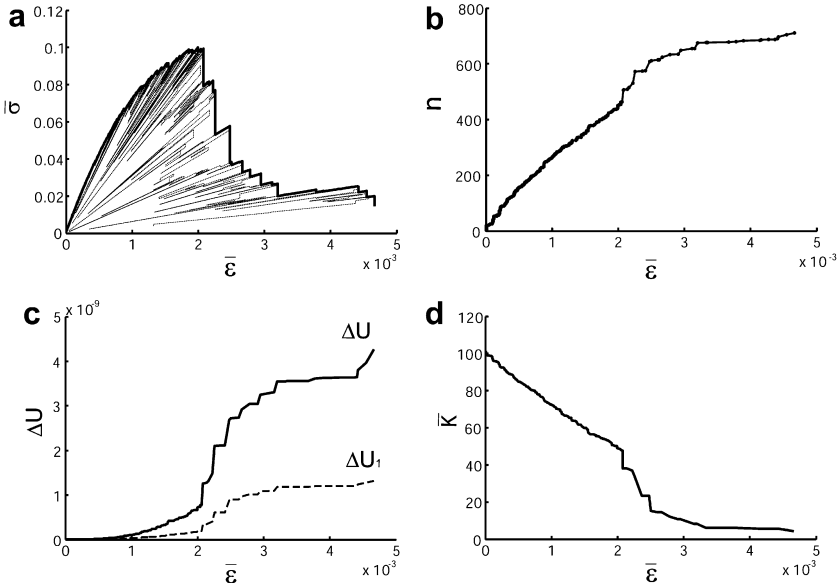


Fig. 3. Results from FE simulation of replicate  $N = 48$ . (a)  $\bar{\sigma}$ – $\bar{\epsilon}$  response in damage (dotted) controlled, displacement controlled (full) line; (b) total broken curve  $n$ – $\bar{\epsilon}$ ; (c) cumulative curve of dissipated strain energy  $\Delta U$  and  $\Delta U_1$ ; (d) secant stiffness curve  $\bar{K}$ – $\bar{\epsilon}$ .

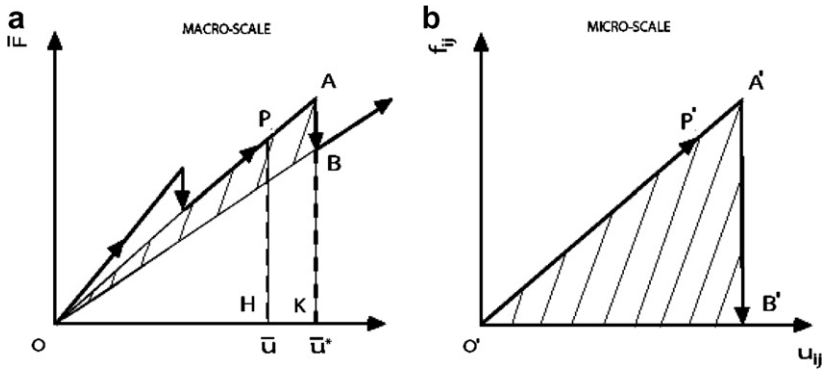


Fig. 4. Energy dissipation due to a single rupture ( $ij$ th link) on the macro- (a) and microscale (b).

$$U = \underbrace{\frac{1}{2} \bar{K} \cdot \bar{u}^2}_{\text{macro-form}} = \underbrace{\frac{1}{2} \mathbf{u}_L^T \mathbf{K}_L \mathbf{u}_L}_{\text{FE-form}} = \underbrace{\frac{1}{2} \sum_{p=1}^{\mathcal{Q}} k_p u_p^2}_{\text{micro-form}} \tag{4}$$

each one expressing different viewpoints. The macro-form is a practical definition that requires only the knowledge of macroscopic quantities (i.e.  $\bar{K}$  and  $\bar{u}$ ) and can be measured graphically as the subtended triangular area of the force–displacement response, such as  $OPH$  in Fig. 4a. This macro-form holds only for uniaxial tests since it is a special case of  $U = \frac{1}{2} \cdot \sum_{m=1}^2 \cdot \sum_{n=1}^2 (\bar{K}_{mnpq} \bar{u}_{pq}) \bar{u}_{mn}$ , with  $\bar{u}_{mn} = \bar{\epsilon}_{mn} L$ , valid for a generic multiaxial loading

scheme in two-dimension where the tensor nature of  $\bar{K}$  and  $\bar{u}$  matters. It carries no knowledge of the strain distribution within the lattice. Conversely, FE-form and micro-form convey the whole knowledge of the field of micro-strains (displacements) but state the same information in terms of different primary variables. The former uses the nodal vectors  $\mathbf{u}_L$  of the  $Z$  nodes and the latter uses the elongation  $u_{(ij)}$  of the  $Q$  active springs. All these forms will be used in the discussion in different moments.

4.1. Individual rupture

Consider now the rupture of the  $p$ th link that happens at  $\bar{u} = \bar{u}^*$  in Fig. 4 when  $\bar{u}$  is controlled. By neglecting dynamical effects, friction or inelastic behaviors other than brittle damage, the passage from state  $A$  to state  $B$  is an instantaneous vertical load drop. The change in strain energy can be expressed from (4) as

$$\Delta U = U^A - U^B = \frac{1}{2}(\bar{K}_A - \bar{K}_B) \cdot \bar{u}^{*2} = \frac{1}{2}\Delta\bar{K} \cdot \bar{u}^{*2} \tag{5}$$

and equals the marked area  $OAB$ . By a microscopic standpoint, instead, one finds that

$$\Delta U = U^A - U^B = \underbrace{\frac{1}{2}k_p u_p^{*2}}_{\Delta U_1} + \underbrace{\frac{1}{2}\sum_{q \neq p}^{Q-1} k_q \Delta(u_q^2)}_{\Delta U_2} = \Delta U_1 + \Delta U_2, \tag{6}$$

where  $u_p^*$  is the critical elongation of the  $p$ th spring. Eq. (6) highlights the existence of two contributions. The first one,  $\Delta U_1$ , is the energy released in the brittle rupturing of the  $p$ th spring and is numerically equal to the area  $O'A'B'$  in Fig. 4b. This information is not usually available from a real test but it is easily obtained in a computer simulation from the a priori detailed knowledge of the microstructure. The second term,  $\Delta U_2$ , is the variation due to the change in the microfield of elongations  $u_q$  ( $q \neq p$ ) when the  $p$ th link is removed. The lattice configuration in  $A$  is no longer equilibrated and local adjustments in the nodal displacements occur to recreate the equilibrium condition of the neighboring links, which is reached at state  $B$ . From the FE-form it is possible to rewrite (6) as

$$\Delta U = U^A - U^B = \frac{1}{2}[(\mathbf{u}_L^T)_A \mathbf{K}_L^A (\mathbf{u}_L)_A - (\mathbf{u}_L^T)_B \mathbf{K}_L^B (\mathbf{u}_L)_B] \tag{7}$$

and then to calculate

$$\Delta U_1 = \frac{1}{2}k_p u_p^{*2} = \frac{1}{2}(\mathbf{u}_L^T)_A (\mathbf{K}_L^A - \mathbf{K}_L^B) (\mathbf{u}_L)_A, \tag{8a}$$

$$\Delta U_2 = \frac{1}{2} \sum_{q \neq p}^{Q-1} k_q \Delta(u_q^2) = (\mathbf{u}_L^T)_A \mathbf{K}_L^B \Delta \mathbf{u}_L - \frac{1}{2} \Delta \mathbf{u}_L^T \mathbf{K}_L^B \Delta \mathbf{u}_L, \tag{8b}$$

where  $\Delta \mathbf{u}_L = (\mathbf{u}_L^A - \mathbf{u}_L^B)$  is the perturbation vector due to damage. Expressions (8) reveal that the redistribution term  $\Delta U_2$  does not have a pre-determined sign while  $\Delta U_1$  is a quadratic positive definite form and  $\Delta U_1 > 0, \forall \mathbf{u}_L^A \neq \mathbf{0}$ . The loss of strain energy  $\Delta U$  can be computed if both stiffness matrices  $\mathbf{K}_L^A$  and  $\mathbf{K}_L^B$  are known.

Variational considerations can be used to enrich the energetic characterization of the damage process. With reference to the irreversible transformation  $A$  to  $B$  in Fig. 4a, the

discrete functional (since  $\mathbf{u}_L$  is not defined on a continuous domain but on a discrete set of  $Z$  nodes)

$$\Pi(\mathbf{u}_L) = U - W = \frac{1}{2} \mathbf{u}_L^T \mathbf{K}_L \mathbf{u}_L - \bar{F} \bar{u} \tag{9}$$

is the potential energy of the lattice at any elastic state (say  $P$  on  $OA$ ). The work potential  $W = F \bar{u}$  (Gurtin, 1975) is zero for a displacement-controlled test. The field  $\mathbf{u}_L$  can be any arbitrary kinematically admissible configuration complying with the given displacement  $\bar{u}$ . The minimization of  $\Pi$  leads to

$$(\partial \Pi / \partial \mathbf{u}_L) = (\partial U / \partial \mathbf{u}_L) = \mathbf{0}, \tag{10}$$

which allows the computation of the only statically admissible (i.e. equilibrated) configuration  $\mathbf{u}_L$ .

4.1.1. The positive sign of  $\Delta U$

It can be demonstrated that  $\Delta U > 0$  regardless of the sign of  $\Delta U_2$ . The difference in potential energy between  $A$  and  $B$  is

$$\Pi^A - \Pi^B = U^A - U^B = \Delta U, \tag{11}$$

where  $\Delta U$  can be expressed as (6) in the FE-form. If none of the passive links becomes active during the rupture of the  $p$ th link in  $A$ , it follows

$$(\mathbf{K}_L^A)_{rs} = \left( \sum_{q \neq p}^{Q-1} \hat{\mathbf{K}}_q^{\text{EL}} + \hat{\mathbf{K}}_p^{\text{EL}} \right)_{rs} = (\mathbf{K}_L^B)_{rs} + (\hat{\mathbf{K}}_p^{\text{EL}})_{rs} \tag{12}$$

for any generic  $rs$ -component of the matrices  $\mathbf{K}_L^A$ ,  $\mathbf{K}_L^B$  and  $\hat{\mathbf{K}}_p^{\text{EL}}$ . The substitution of (12) into (9) leads to the inequality

$$\Pi^A = U^A = \frac{1}{2} [(\mathbf{u}_L^T)_A \mathbf{K}_L^{\text{EL}}(\mathbf{u}_L)_A + (\mathbf{u}_L^T)_A \mathbf{K}_L^B(\mathbf{u}_L)_A] > \frac{1}{2} (\mathbf{u}_L^T)_A \mathbf{K}_L^B(\mathbf{u}_L)_A. \tag{13}$$

If the lattice configurations  $\mathbf{u}_L^A$  and  $\mathbf{u}_L^B$  are the solutions of (10) for  $A$  and  $B$  respectively, then it must be

$$\Pi^B = U^B = \frac{1}{2} [(\mathbf{u}_L^T)_B \mathbf{K}_L^B(\mathbf{u}_L)_B] < \frac{1}{2} (\mathbf{u}_L^T)_A \mathbf{K}_L^B(\mathbf{u}_L)_A, \tag{14}$$

because  $\mathbf{u}_L^A$  is kinematically admissible but not equilibrated and the minimum of the functional  $\Pi(\mathbf{u}_L) = \frac{1}{2} \mathbf{u}_L^T \mathbf{K}_L^B \mathbf{u}_L$  corresponds to  $\mathbf{u}_L^B$ . Therefore, from (13) and (14) the following inequality holds

$$\Pi^A > \frac{1}{2} (\mathbf{u}_L^T)_A \mathbf{K}_L^B(\mathbf{u}_L)_A > \Pi^B, \tag{15}$$

which is the rigorous proof that  $\Delta U > 0$  and  $\Delta \bar{K} > 0$  in (5) and (11).

4.1.2. Maximum dissipation principle for  $\Delta \Pi$

The perturbation field  $\Delta \mathbf{u}_L$  is constrained by a “maximum” variational principle. By assuming that  $\mathbf{u}_L^B$  is unknown unlike  $\{\mathbf{u}_L^A, \mathbf{K}_L^A, \mathbf{K}_L^B\}$ , then  $\Pi^A$  is also known. The field  $\mathbf{u}_L^B$  that minimizes  $\Pi^B$  is the solution that also maximizes the functional difference  $\Delta \Pi(\mathbf{u}_L^B) = (\Pi^A - \Pi^B)$ , i.e.

$$\frac{\partial (\Pi^A - \Pi^B)}{\partial \mathbf{u}_L^B} = \frac{\partial (\Delta U)}{\partial \mathbf{u}_L^B} = 0. \tag{16}$$

By substituting  $\mathbf{u}_L^B = \mathbf{u}_L^A - \Delta\mathbf{u}_L$  as in (8b) and using the chain rule, the derivative (16) can be expressed directly in terms of the perturbation field as

$$\frac{\partial(\Delta U)}{\partial(\Delta\mathbf{u}_L)} = \frac{\partial(\Delta U_2)}{\partial(\Delta\mathbf{u}_L)} = 0 \quad (17)$$

and finally as

$$\mathbf{K}_L^B \Delta\mathbf{u}_L = \mathbf{K}_L^B \mathbf{u}_L^A. \quad (18)$$

The right hand side of (18) represents the disequilibrium (force) caused by the rupture and constitutes the driving force of the perturbation  $\Delta\mathbf{u}_L$ . From Eqs. (10) and (12) one deduces that all the elements of the vector  $\mathbf{K}_L^B \mathbf{u}_L^A$  are the same as  $\mathbf{K}_L^A \mathbf{u}_L^A$  besides the four *dof* of the broken *p*-link. Since  $\mathbf{K}_L^A \mathbf{u}_L^A$  represents the equilibrated state A of the lattice with external forces applied only at the boundary nodes, all the components of  $\mathbf{K}_L^B \mathbf{u}_L^A$  are zeros except for the *dof* of the *p*-link (disequilibrium) and to the outer nodes (external support reactions in state A). Therefore a local perturbation associated to the disequilibrium of four *dof* governs the transformation from A to B.

*Variational principle of maximum dissipation:* the elastic perturbation field due to the introduction of new damage in the lattice maximizes the drop of potential energy  $\Delta\Pi$  from state A to state B.

The variational formulation might become useful to implement an incremental approach when the new equilibrated state B needs to be computed from state A rather than from O in Fig. 4a. A similar situation is encountered in presence of damage-plasticity or when an approximate solution is sought by updating the previous undamaged configuration in a sub-domain where the perturbation field  $\Delta\mathbf{u}_L$  exceeds a threshold value, e.g. in very large lattices and during damage propagation. The perturbation, in purely elastic networks like this one, practically spans the whole lattice during hardening but is confined in a smaller area when damage localizes.

#### 4.1.3. Load redistribution effect $\Delta U_2$

The meaning of the redistribution term  $\Delta U_2$ , as defined in (6) or (8b), deserves further attention. This quantity accounts for the interaction effect between a single structural element and the surrounding, which characterizes higher dimensional and highly interconnected systems, such as real microstructures. For instance, the simplest one-dimensional statistical model, the parallel bars system, does not have a  $\Delta U_2$  term and  $\Delta U = \Delta U_1$ . From (8b), two components contribute to  $\Delta U_2$ . The first term  $(\mathbf{u}_L^T)_A \mathbf{K}_L^B \Delta\mathbf{u}_L$  is the work of the non-equilibrium forces introduced in the system by the deletion of the *p*th link. The  $\mathbf{K}_L^B \mathbf{u}_L^A$  vector has been already identified in (18) as the source of perturbation. More precisely, the disequilibrium corresponds to the force pair  $\vec{F}_i$  and  $\vec{F}_j$  shown in Fig. 5, which pull the node *i* and *j* away from each other. When the lattice configuration is  $\mathbf{u}_L^A$  and the *p*th link is removed, only these two forces perform work on the corresponding nodal perturbation vectors  $\Delta\mathbf{u}_i = [\Delta u_i \quad \Delta v_i]^T$  and  $\Delta\mathbf{u}_j = [\Delta u_j \quad \Delta v_j]^T$ . Consequently,  $(\mathbf{u}_L^T)_A \mathbf{K}_L^B \Delta\mathbf{u}_L > 0$ . The intensity of  $\vec{F}_i$  and  $\vec{F}_j$  is not constant in reality but the transition to the new equilibrated state B is instantaneous in this mathematical model.

On the other hand, the second component of  $\Delta U_2$ , i.e.  $-1/2 \Delta\mathbf{u}_L^T \mathbf{K}_L^B \Delta\mathbf{u}_L$ , is always negative because  $\Delta\mathbf{u}_L^T \mathbf{K}_L^B \Delta\mathbf{u}_L$  is a positive definite form. Therefore, while the energy  $(\mathbf{u}_L^T)_A \mathbf{K}_L^B \Delta\mathbf{u}_L$  associated to the disequilibrium is spent to reach the new configuration, part of it is stored into the neighboring springs. Even if some links relax and other carry higher

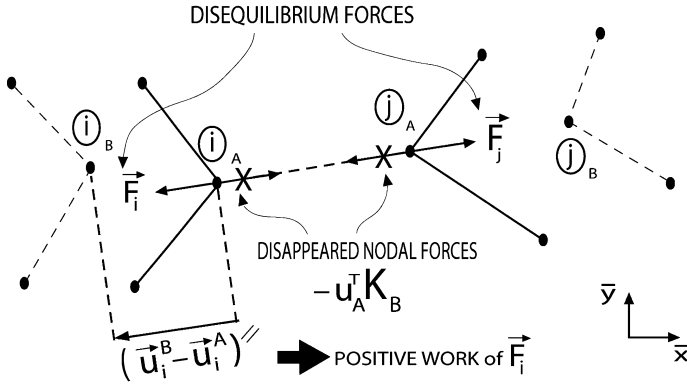


Fig. 5. Disequilibrium generated by deletion of  $ij$ th spring in the configuration  $A$  (full) and new stable configuration  $B$  (dashed).

load, there is always such partial gain/recovery of strain energy. The local details of the disordered microstructure determine the redistribution capability. In conclusion  $\Delta U_2$  is a trade-off between these two counter actions and the sign  $\Delta U_2$  cannot be predicted a priori. Simulations indicate that the area  $OAB$  is most of the time greater than  $O'A'B'$  in Fig. 4 but not always, i.e.  $\Delta U > \Delta U_1$  most frequently. Fig. 3c shows the cumulative curves of  $\Delta U$  (full line) and  $\Delta U_1$  (dashed line). The divergence between the two curves becomes more visible at the transition and in the softening phase, where  $\Delta U_2$  plays a dominant role.

4.2. Cascade of ruptures: avalanche and snapback

The results for the individual rupture can be extended to the general case of multiple ruptures by introducing the concept of “avalanche”. An avalanche consists of a cascade of ruptures of more links in correspondence of the same value  $\bar{u}$  in the displacement-controlled process. The order of the avalanche is the number of ruptures. One example of an order 3 avalanche is shown schematically in Fig. 6. The avalanche is an instability phenomenon occurring when the new equilibrated lattice configuration  $\mathbf{u}_L^B$  in (7), reached after the first rupture, is kinematically admissible but incompatible with the lattice strength. In fact the perturbation field associated to the load redistribution can drive at

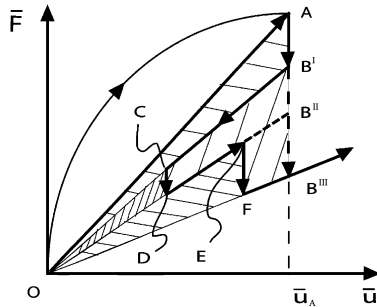


Fig. 6. Avalanche of order 3 and snapback effect between states  $A$  and  $B$  (i.e.  $B^{III}$ ).

least one more link to exceed its critical strain under the same imposed displacement  $\bar{u}$ . A strong perturbation effect can also involve links of superior strength in the avalanche. Avalanches do not occur in a damage-controlled situation, when  $\bar{u}$  is a dependent variable and the lattice is allowed to “snapback” to the equilibrated state determined by the element of highest affinity as explained before. Snapbacks due to avalanches are visible in the damage-controlled response in Fig. 3a (dotted lines) and denote massive energy redistribution. The gap between  $\Delta U$  and  $\Delta U_1$  (Fig. 3c) increases particularly in correspondence of the large avalanches in the softening phase.

By an energetic standpoint, an extra term  $\Delta U_3$  must be added in the balance (6) for each link in the avalanche to account for the extra dissipation associated to the snapback. The total drop of strain energy for an avalanche of order  $q$  between state  $A$  and  $B$  is simply the sum of the  $q$  contributions

$$\Delta U = U_A - U_B = \sum_{i=1}^q (\Delta U_1 + \Delta U_2 + \Delta U_3)_i. \tag{19}$$

Under the assumption of instantaneous load redistribution and no dynamic and frictional effects, the lattice would tend to follow the “pattern of minimum energy”  $A - B - C - D - E - F - B^{III}$  from  $A$  in Fig. 6 but it is constrained to stay at  $\bar{u}_A$  and, hence, it is forced into the non-equilibrium pattern  $A - B^I - B^{II} - B^{III}$ . The snapback effect is approximately represented by the area enclosed by the closed loop  $B^I - C - D - E - F - B^{III}$ . For the second rupture, for example,  $\Delta U_3$  coincides with the area of the polygon  $B^I - C - D - B^{II}$  and can be computed as

$$\Delta U_3^{(2)} = \frac{1}{2} [\bar{u}_A^2 \Delta \bar{K}_{B^I B^{II}} - \bar{u}_C^2 \Delta \bar{K}_{CD}]. \tag{20}$$

The geometrical similarity between triangles  $OCD$  and  $OB^I B^{II}$  introduces the proportionality factor

$$\lambda^{(2)} = \frac{\Delta \bar{K}_{B^I B^{II}}}{\Delta \bar{K}_{CD}} = \frac{\bar{u}_A}{\bar{u}_C} = \frac{\bar{u}_1}{\bar{u}_2}. \tag{21}$$

Since  $1/2 \cdot \bar{u}_C^2 \Delta \bar{K}_{CD}$  is the effect of  $\Delta U_1^{(2)}$  and  $\Delta U_2^{(2)}$  related to the second rupture, it follows from (5) and (6) that

$$\Delta \bar{K}_{CD} = \frac{2(\Delta U_1^{(2)} + \Delta U_2^{(2)})}{\bar{u}_C^2}. \tag{22}$$

Finally, by generalizing to any  $i$ th rupture in the avalanche with  $i = 1, \dots, q$ , the substitution of (21) and (22) into (20) gives

$$\Delta U_3^{(i)} = \left( \left( \frac{\bar{u}_1}{\bar{u}_i} \right)^2 - 1 \right) (\Delta U_1^{(i)} + \Delta U_2^{(i)}) = (\lambda_i^2 - 1) (\Delta U_1^{(i)} + \Delta U_2^{(i)}), \tag{23}$$

where  $\bar{u}_1 = \bar{u}_A$  and  $\bar{u}_2 = \bar{u}_C$  for  $i = 2$  (Fig. 6). The parameter  $\lambda_i = \bar{u}_1/\bar{u}_i$  conveys the effect of the snapback for any  $i$ th rupture in the avalanche. Since  $\bar{u}_1 \geq \bar{u}_i$ , it is always  $\lambda_i > 1$  and  $\Delta U_3^{(i)} = 0$  if there is no snapback, like in the first rupture. However, the quota  $\Delta U_3^{(i)}$  is proportional to  $\lambda_i^2$  and is potentially much larger than  $(\Delta U_1^{(i)} + \Delta U_2^{(i)})$  if the snapback is marked, e.g. at the peak. The observed energy loss  $\Delta U^{(i)}$  during the load-drop  $B^{i-1} B^i$  is from (23)

$$\Delta U^{(i)} = \Delta U_1^{(i)} + \Delta U_2^{(i)} + \Delta U_3^{(i)} = \lambda_i^2(\Delta U_1^{(i)} + \Delta U_2^{(i)}) > 0. \tag{24}$$

Therefore, the snapback simply causes an *amplification* of the energy dissipated in a single rupture. Finally, the total observed energy drop  $AB$  and the total snapback contributions are respectively

$$\Delta U = U_A - U_B = \sum_{i=1}^p \Delta U^{(i)} = \sum_{i=1}^p [\lambda_i^2(\Delta U_1^{(i)} + \Delta U_2^{(i)})] > 0, \tag{25}$$

$$\text{and } \Delta U_3^{\text{TOT}} = \sum_{i=1}^p \Delta U_3^{(i)} = \sum_{i=1}^p [(\lambda_i^2 - 1)(\Delta U_1^{(i)} + \Delta U_2^{(i)})] \geq 0. \tag{26}$$

Unfortunately  $\lambda_i$ ,  $\Delta U_1^{(i)}$  and  $\Delta U_2^{(i)}$  are random quantities and are “hidden” on the macro-scale, where only  $\Delta U$  is usually observable. The experimental assessment of the cumulative snapback effect  $\Delta U_3^{\text{TOT}}$  for an avalanche is indeed a challenging task. Reliable numerical simulations are likely the best tool for this kind of investigation. In conclusion the non-equilibrium pattern  $A - B^I - B^{II} - B^{III}$  is the pattern of minimum energy dissipation compatible with the microstructure and with the imposed kinematical constraint  $\bar{u}_A$ . Simulations show that the snapback pattern is a random variable dependent on the microstructural disorder and requires a statistical characterization from many random realizations. The extra energy term  $\Delta U_3^{\text{TOT}}$  is associated to the non-equilibrium pattern  $A - B^I - B^{II} - B^{III}$  at  $\bar{u}$ . The energy drop  $\Delta U$  in (25) is always positive and is maximized by the perturbation field associated to the avalanche.

Evidently from Figs. 3a and 7b for  $N = 48$ , large avalanches characterize the critical point (the stress peak), where the homogeneous–heterogeneous transition occurs, and cause marked load drops in the response. The order of the avalanche is an indicator of the range of interaction between defects and Fig. 7 demonstrates that the correlation length at the onset of the transition is of the order of the lattice size  $L$ . A diverging correlation length at force peak is consistent with the general phenomenology of phase transitions, where certain thermodynamic parameters and the correlation length diverge at the critical points. For  $N = 192$  in Fig. 7c the magnitude of the avalanches jumps from few units to about 400 and 1200 in correspondence to the critical point. After the sharp transition, the lattice cannot reach a configuration compatible with the imposed displacement. In cases such as this one no softening phase exists and catastrophic failure occurs suddenly at the stress peak. The failure can happen either stably with the isolated rupture of a single element or during an avalanche.

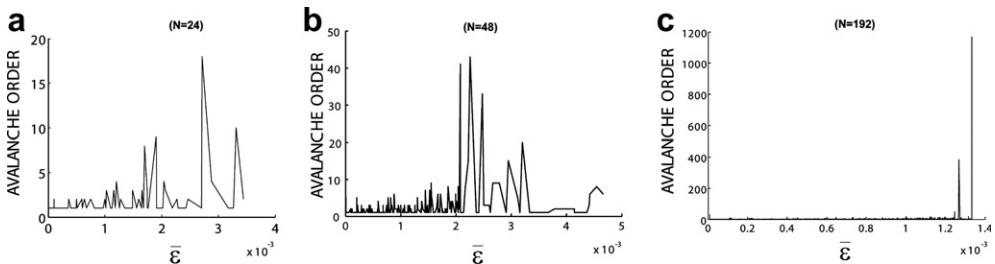


Fig. 7. Evolution of order of avalanche for replicates  $N = \{24, 48, 192\}$ . Diverging avalanches are observed at the peak transition.

## 5. Statistical foundations of $\bar{D}$ during hardening

This section investigates the statistical foundations of the definition (2) of  $\bar{D}$  drawn from empirical arguments. The theory is developed for honeycomb lattices with random mechanical properties only. This responds, in first place, to a “blocking” strategy used in statistics to eliminate the bias due to geometrical disorder and to make the mechanical disorder the only source of variability in the lattice response. Secondly, the exact triangular lattice (with equal spring constants) in pristine state maps into an isotropic continuum element, as shown by Monette and Anderson (1994), and is convenient to study the development of anisotropic damage. Thirdly, the perfect geometry introduces the important simplification of just three spring orientations  $\theta = \{0^\circ, 60^\circ, -60^\circ\}$  with respect to the loading axis  $\bar{x}$ . This configuration is sufficient to develop clear arguments that can be generalized at a later time for a disordered texture. Due to the symmetry of the diagonal elements, we partition the springs into two groups:

1. Group 1: the set of  $N_1$  horizontal links ( $\theta = 0^\circ$ ).
2. Group 2: the set of  $N_2$  diagonal links ( $\theta = \{60^\circ, -60^\circ\}$ ).

For the lattice in Fig. 1a, a counting exercise demonstrates that  $N_1 = N \cdot (N - 1) - \text{trunc}(N/2)$  and  $N_2 = 2 \cdot N \cdot (N - 1)$ , whose sum is equal to the total number of springs  $N_0$  and which are approximated in the asymptotic limit of  $N \rightarrow \infty$  by

$$N_1 = 1/3 \cdot N_0, \quad (27a)$$

$$N_2 = 2/3 \cdot N_0. \quad (27b)$$

This is a good approximation already for  $N = 24$  and we will adopt it. A rational model for  $\bar{D}(\bar{\varepsilon}, L)$  is derived for the hardening phase under the assumption that only individual rupture events occur. The generalization of this framework to the softening phase and to avalanches is actually straight forward and will be the object of another submission in preparation.

The energy loss  $\Delta U$  due to the failure of the  $p$ th spring is given by (6) from the sum of  $\Delta U_1 = k_p u_p^{*2}$ , estimable a priori from knowledge of  $\{k_p, u_p^*\}$ , and  $\Delta U_2$ , which is unknown. To express  $\Delta U_2$  in terms of  $\Delta U_1$ , we define the redistribution factor  $\eta_p$

$$\eta_p = \frac{\Delta U_2}{\Delta U_1} = \frac{\Delta U - \Delta U_1}{\Delta U_1} \quad (28)$$

and the  $\Delta U$  can be rewritten as

$$\Delta U = (1 + \eta_p)\Delta U_1 = \frac{1}{2}(1 + \eta_p)k_p u_p^{*2}, \quad (29)$$

where  $\eta_p > -1$  is the only prescription on  $\eta_p$  from  $\Delta U > 0$ . Since the macro-form (5) holds for uniaxial loading, the loss of secant stiffness  $\Delta \bar{K}$  is

$$\Delta \bar{K} = \frac{(1 + \eta_p)k_p u_p^{*2}}{\bar{u}^{*2}}. \quad (30)$$

Because all springs have same length  $\ell_{(ij)} = \ell_0$  ( $\ell_0 = 1$  in this model) and stiffness  $k_{(ij)} = k$ , the lattice and link strains are respectively

$$\bar{\varepsilon}^* = \bar{u}^*/L \quad \text{and} \quad \varepsilon_{(ij)}^* = \mathbf{u}_{(ij)}^*/\ell_0, \tag{31}$$

whose substitution in (30) renders

$$\Delta\bar{K} = (1 + \eta_p)k \left(\frac{\ell_0}{L}\right)^2 \left(\frac{\varepsilon_p^*}{\bar{\varepsilon}^*}\right)^2. \tag{32}$$

According to the simulation data in Fig. 8 for  $N = \{24, 48, 192\}$ ,  $\eta_p$  varies sensibly during the damage process but has an average value around  $\eta_p \simeq 2.2$  in the beginning of the hardening phase. The correlation between link orientation  $\theta_p$  and  $\eta_p$  is overlooked and  $\eta_p$  is assumed to be insensitive to the orientation in this paper. For the sake of simplicity, we also assume  $\eta_p = 2$  and Eq. (32) becomes

$$\Delta\bar{K} = 3k \left(\frac{\ell_0}{L}\right)^2 \left(\frac{\varepsilon_p^*}{\bar{\varepsilon}^*}\right)^2. \tag{33}$$

The robustness of the results to this approximation has been verified against numerical data. The damage parameter  $\bar{D}(\bar{\varepsilon})$  estimates the cumulative effect of the  $n(\bar{\varepsilon})$  ruptures at  $\bar{\varepsilon}$  and from (33)

$$\bar{D}(\bar{\varepsilon}) = \frac{\Delta\bar{K}_{\text{TOT}}}{\bar{K}_0} = \frac{\sum_{p=1}^{n(\bar{\varepsilon})} \Delta\bar{K}_p}{\bar{K}_0} = \frac{3k}{\bar{K}_0} \left(\frac{\ell_0}{L}\right)^2 \sum_{p=1}^{n(\bar{\varepsilon})} \left(\frac{\varepsilon_p^*}{\bar{\varepsilon}^*}\right)^2. \tag{34}$$

$\bar{D}(\bar{\varepsilon})$  can be computed if  $\varepsilon_p^*$  and  $\bar{\varepsilon}^*$  are known for the all  $n(\bar{\varepsilon})$  springs. Nevertheless,  $\varepsilon_p^*$  is a microscopic random variable from the selected quenched distribution, and  $\bar{\varepsilon}^*$  is a macroscopic random variable that depends in a non-trivial manner on  $\varepsilon_p^*$  and on the interaction range between ruptures. Hence, damage is a stochastic process and  $\bar{D}(\bar{\varepsilon})$  is a random variable itself. By partitioning the total number of ruptures  $n(\bar{\varepsilon})$  into the three subsets  $\{n_1(\bar{\varepsilon}), n_2(\bar{\varepsilon}), n_3(\bar{\varepsilon})\}$  along  $\theta = \{0^\circ, 60^\circ, -60^\circ\}$  respectively

$$n(\bar{\varepsilon}) = n_1(\bar{\varepsilon}) + n_2(\bar{\varepsilon}) + n_3(\bar{\varepsilon}). \tag{35}$$

Eq. (34) can be written as

$$\bar{D}(\bar{\varepsilon}) = \frac{3k}{\bar{K}_0} \left(\frac{\ell_0}{L}\right)^2 \left[ \sum_{p1=1}^{n_1(\bar{\varepsilon})} \left(\frac{\varepsilon_{p1}^*}{\bar{\varepsilon}^*}\right)^2 + \sum_{p2=1}^{n_2(\bar{\varepsilon})} \left(\frac{\varepsilon_{p2}^*}{\bar{\varepsilon}^*}\right)^2 + \sum_{p3=1}^{n_3(\bar{\varepsilon})} \left(\frac{\varepsilon_{p3}^*}{\bar{\varepsilon}^*}\right)^2 \right]. \tag{36}$$

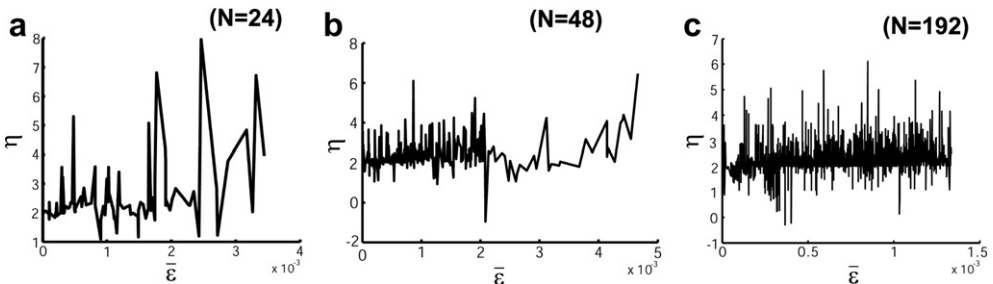


Fig. 8. Redistribution factor  $\eta$  for replicates  $N = \{24, 48, 192\}$ . The assumption  $\eta \simeq 2$  in the hardening phase is more accurate as the lattice size increases. The replicate  $N = 192$  does not have a softening phase.

This equation yields accurate results for  $\overline{D}(\bar{\epsilon})$  if the input parameters  $\{\bar{\epsilon}_{pi}^*/\bar{\epsilon}^*, n_i(\bar{\epsilon})\}$  from simulations were collected and used directly for individual lattices.

5.1. A closed form model for  $\langle \overline{D}(\bar{\epsilon}) \rangle$

An analytical relation for average  $\langle \overline{D}(\bar{\epsilon}) \rangle$  of broader statistical valence, unrestrained from any specific replicate, will be derived from expression (36). The following set of assumptions is adopted for this purpose:

1. the lattice is much larger than the link length,  $L \gg \ell_0$  and is treated as an infinitesimal Cauchy element of isotropic material having Young’s modulus  $E = \overline{K}_0$  and Poisson’s ratio  $\nu$ ,
2. the small strains associated to the Cauchy element are small,
3. the rupturing process consists of one *independent* process for Group 1 ( $\theta = 0^\circ$ ) and of another *dependent* process for Group 2 ( $\theta = \{60^\circ, -60^\circ\}$ ); this dependency is “one-way correlated” since the latter is influenced by former without influencing it in return (ref. Section 5.1.1),
4. the rupturing process on each orientation is not spatially *autocorrelated* (ref. Section 5.1.1),
5. the threshold  $\bar{\epsilon}_p^*$  for each orientation are sampled independently of each other from the same quenched distribution,
6. only a subset  $N_2^* \leq N_2$  of the diagonal links is subjected to a significant tensile perturbation induced by the horizontal ruptures and participates to the damage process; on an experimental basis the active set is assumed to be

$$N_2^* = N_2/6 = N_1/3. \tag{37}$$

The first two assumptions imply that for any applied  $\bar{\epsilon}$  the mean strain field in the lattice is expressed in global coordinates (Fig. 1a) by the small-strains tensor

$$\mathbf{E}_{xy} = \begin{vmatrix} \bar{\epsilon}_{xx} & \bar{\epsilon}_{xy} \\ \bar{\epsilon}_{xy} & \bar{\epsilon}_{yy} \end{vmatrix} = \begin{vmatrix} \bar{\epsilon} & 0 \\ 0 & -\nu \cdot \bar{\epsilon} \end{vmatrix}. \tag{38}$$

The Poisson’s ratio is about  $\nu = 0.33$  for our lattices with greater accuracy for  $N > 48$ . The strain field can be represented in any other local frame  $x'-y'$  via the transformation  $\mathbf{E}_{x'y'}(\phi) = \mathbf{R}^T(\phi)\mathbf{E}_{xy}\mathbf{R}(\phi)$ , where  $\phi$  is the inclination of  $x'$  in  $x-y$  and  $\mathbf{R}(\phi)$  is the rotation matrix around the  $z$ -axis. Therefore, for  $\phi = 60^\circ$  (or  $\phi = -60^\circ$ ) it follows:

$$\mathbf{E}_{x'y'}(\phi = 60^\circ) = \frac{\bar{\epsilon}}{4} \begin{vmatrix} 1 - 3\nu & \sqrt{3}(1 + \nu) \\ \sqrt{3}(1 + \nu) & 3 - \nu \end{vmatrix}. \tag{39}$$

The components  $\bar{\epsilon}_{xx}$  in (38) and  $\bar{\epsilon}_{x'x'}$  in (39) are the mean-field estimates of the strain level in the horizontal and diagonal links respectively. Thus, a possible simplified relation between the kinematics on the macroscale and on the microscale would be

$$\varepsilon_{(ij)}(\theta = 0^\circ) = \langle \varepsilon_{(ij)}(\theta = 0^\circ) \rangle = \bar{\varepsilon}_{xx} = \bar{\varepsilon}, \tag{40a}$$

$$\varepsilon_{(ij)}(\theta = \pm 60^\circ) = \langle \varepsilon_{(ij)}(\theta = \pm 60^\circ) \rangle = \bar{\varepsilon}_{x'x'} = \frac{1 - 3\nu}{4} \bar{\varepsilon}. \tag{40b}$$

However, this turns out to be not entirely correct since the fluctuations in the  $\varepsilon_{(ij)}$  micro-field due to finite lattice size and microcracks are neglected while they play a fundamental role. This can be demonstrated from the examination of simulation data. The strain levels in the horizontal and diagonal links are Gaussian-like distributed random variables already in the pristine state because of the finite lattice size and the presence of free boundaries. Fig. 9 displays the three plots tracking maximum, mean, and standard deviation of the strain distributions of horizontal (full line) and 60° diagonal (dashed line) for  $N = 48$  over the entire damage process. The vertical drops observable in the plots denounce multi-valued estimates in correspondence to avalanches of order greater than one. In the hardening phase, away from the peak, the plot in Fig. 9a confirms that the average strain level in the horizontal links is approximately equal to the macro strain, as hypothesized in (40a). The large difference between the mean values of Group 1 and Group 2 is also evident. The ratio between the two mean values, plotted in Fig. 10a for this simulation, indicates that the average strain level in the horizontal links is approximately two orders of magnitude (OM) greater than in the diagonals throughout the damage process, with a peak-ratio of about 550 in the limit of zero damage. On the contrary, the exam of the maximum strain values in Fig. 9c reveals that the difference between the maximum strains in the two Groups of links is not as large as for the means. According to the plot of the ratio between the maximum strains in Fig. 10b, these quantities are indeed of the same OM. Instead, the ratio maximum-to-mean strain plotted in Fig. 10c shows two OM difference between maximum and mean strains for the diagonals. Thus, while most of the diagonal links are at strain levels of the same OM than the mean-field estimate (40b), a smaller set is subject strain levels one OM higher. In conclusion, the kinematical assumption (40) is accurate for the horizontal links but is too simplistic for the diagonals. The values of standard deviation of the diagonal links in Fig. 9b are clearly inflated by this process and could be misinterpreted if such partition within diagonals were overlooked and if the standard deviations of diagonal and horizontal distributions were compared directly.

A quantitative measure of the influence of the rupturing process on the microscale kinematics is possible from the plots of the percent perturbation fields produced by the first

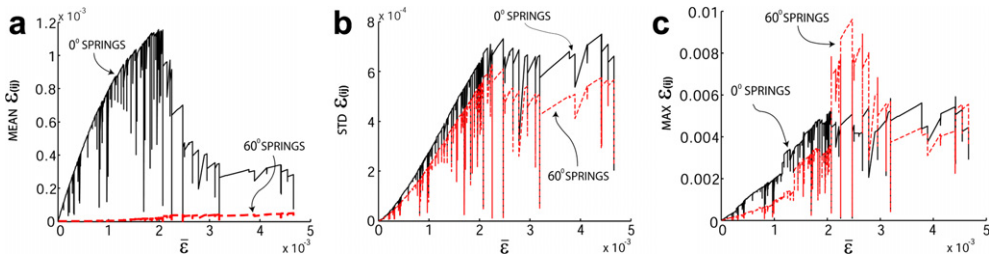


Fig. 9. Plots of the mean (a), standard deviation (b) and maximum (c) of the  $\varepsilon_{(ij)}$  distribution vs.  $\bar{\varepsilon}$  of survival horizontal (solid) and 60° diagonal (dashed) links for the replicate  $N = 48$ . The last plot shows the crossover in correspondence of the transition where diagonal springs experience a higher value of maximum strain.

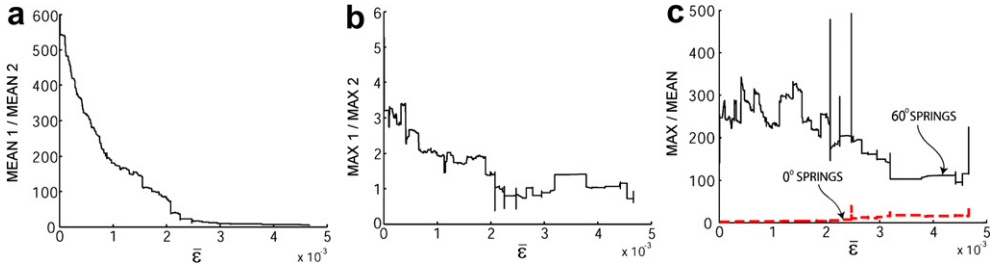


Fig. 10. (a) Ratio between the mean of microstrains  $\varepsilon_{(ij)}$  of horizontal and diagonal links, (b) ratio between the maximum strains  $\varepsilon_{(ij)}$  in horizontal and diagonal links and (c) ratio max-to-mean per horizontal and  $60^\circ$  diagonal for the replicate  $N = 48$ .

rupture of one horizontal link in Fig. 11. The percent perturbation for the  $ij$ th unbroken element is computed as

$$\% \text{ Strain Perturbation} = \frac{\varepsilon_{(ij)} - \varepsilon_{(ij)}^{\text{REF}}}{\varepsilon_{(ij)}^{\text{REF}}} \times 100, \tag{41}$$

where  $\varepsilon_{(ij)}^{\text{REF}}$  is the strain of the  $ij$ th spring measured under the same macrostrain  $\bar{\varepsilon}$  if the lattice were in pristine condition. The magnitude of the perturbation decays away from the damaged location but the maximum tensile perturbation induced on diagonal links is  $10^3$ – $10^4\%$ , against the 20% of the horizontal links. Such a remarkable amplification of the strain field of the diagonal links is certainly capable of “triggering” the ruptures of the weaker diagonal elements. Maxima and minima are localized in the proximity of the rupture. Then, going back to our set of assumptions, the third one expresses such “trigger” action of the ruptures in Group 1 on Group 2, whereas the sixth assumption means that only the ruptures of diagonal links piloted by Group 1 are relevant to the model. The damage process in the other diagonal links, unexposed to a significant tensile perturbation, is too slow and negligible for the purposes of our derivation. Therefore, by letting the

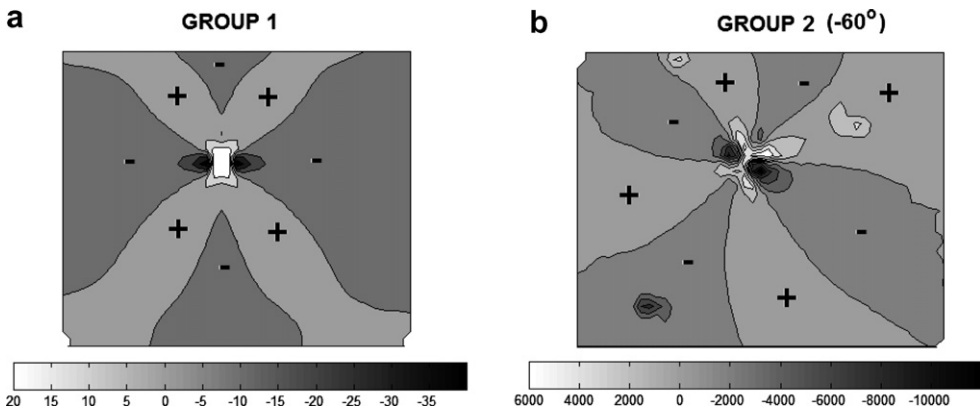


Fig. 11. Percent perturbation fields in survivor horizontal (a) and diagonal at  $-60^\circ$  links (b) produced by the first (horizontal) rupture for  $N = 24$ .

strain field in the “active” diagonal elements be of the same order of Group 1 reflecting the maximum in Fig. 9c, Eq. (40b) is replaced by the following “maximum-field” estimate

$$\varepsilon_{(ij)}(\theta = \pm 60^\circ) = \langle \varepsilon_{(ij)}(\theta = 0^\circ) \rangle = \bar{\varepsilon}. \tag{42}$$

Of course, the mean-field approximation (40a) for Group 1 is retained unchanged because there was no evident converse influence of Group 2 onto Group 1.

Eqs. (40a) and (42) introduce a perfect (linear) correlation between the random pair  $\varepsilon_p^*$  and  $\bar{\varepsilon}^*$  in (36) for all three orientations when a link reaches the rupturing condition  $\varepsilon_{(ij)} = \varepsilon_{(ij)}^*$ . The most important consequence is that the random variable  $\varepsilon_{(ij)}^*/\bar{\varepsilon}^*$  becomes deterministic and Eq. (36) simplifies as

$$\begin{aligned} \bar{D}(\bar{\varepsilon}) &= \frac{3k}{\bar{K}_0} \left(\frac{\ell_0}{L}\right)^2 \left[ \sum_{p1=1}^{n_1(\bar{\varepsilon})} (1)^2 + \sum_{p2=1}^{n_2(\bar{\varepsilon})} (1)^2 + \sum_{p3=1}^{n_3(\bar{\varepsilon})} (1)^2 \right] \\ &= \frac{3k}{\bar{K}_0} \left(\frac{\ell_0}{L}\right)^2 [n_1(\bar{\varepsilon}) + n_2(\bar{\varepsilon}) + n_3(\bar{\varepsilon})]. \end{aligned} \tag{43}$$

Nevertheless,  $\bar{D}(\bar{\varepsilon})$  is still random like  $n_1(\bar{\varepsilon})$ ,  $n_2(\bar{\varepsilon})$  and  $n_3(\bar{\varepsilon})$ . The expected value  $\langle \bar{D}(\bar{\varepsilon}) \rangle$  can be calculated from the knowledge of the quenched distribution for  $\varepsilon_{(ij)}^*$  by virtue of the fifth assumption. The values  $\varepsilon_p^*$  are sampled from the uniform distribution with the probability density function  $p(\varepsilon_p) = 1/\varepsilon^{\text{MAX}}$  shown in Fig. 12. The rupturing probability of the  $p$ th link at  $\bar{\varepsilon}$  is

$$P(\varepsilon_p^* < \varepsilon_p(\bar{\varepsilon}, \theta_p)) = P(\bar{\varepsilon}, \theta_p) = \int_0^{\varepsilon_p(\bar{\varepsilon})} p(\varepsilon) d\varepsilon = \frac{\varepsilon_p(\bar{\varepsilon}, \theta_p)}{\varepsilon^{\text{MAX}}}, \tag{44}$$

with  $\varepsilon_p$  given by either (40a) or (42) for Groups 1 and 2 respectively. Since the links at  $60^\circ$  and  $-60^\circ$  have same rupturing probability, the ratio between the probabilities  $P_1 = P(\bar{\varepsilon}, \theta_p = 0^\circ)$  and  $P_2 = P(\bar{\varepsilon}, \theta_p = \pm 60^\circ) = 2 \cdot P(\bar{\varepsilon}, \theta_p = 60^\circ) = 2 \cdot P_1(\bar{\varepsilon})$  of these Groups is

$$\frac{P_1(\bar{\varepsilon}, \theta_p = 0^\circ)}{P_2(\bar{\varepsilon}, \theta_p = \pm 60^\circ)} = \frac{1}{2}. \tag{45}$$

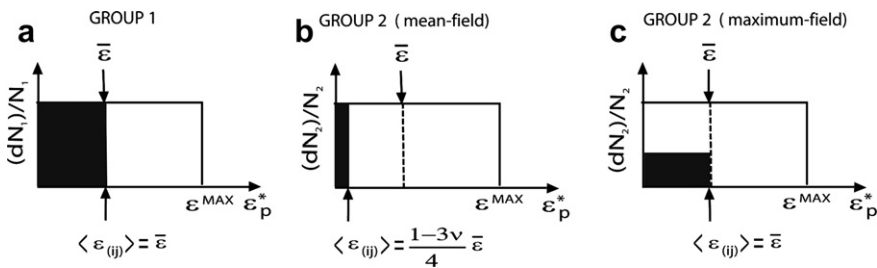


Fig. 12. Schematic representations of the probability (shaded area) of sampling a critical value  $\varepsilon_p^*$  less than the average microstrain  $\langle \varepsilon_{(ij)} \rangle$  for the given  $\bar{\varepsilon}$  with respect to the selected quenched distribution. The three plots are a pictorial representation of the kinematic assumptions (40) and (42) relating the values  $\langle \varepsilon_{(ij)} \rangle$  and  $\bar{\varepsilon}$ . While (a) refers to Group 1, other schemes indicate the failure probability of a diagonal link in Group 2 according to mean-field (b) and maximum-field estimates (c).

From the fifth assumption and Eq. (40a), the set of  $N_1$  threshold values  $\varepsilon_p^*(\theta_p = 0^0)$  of Group 1 forms at any given  $\bar{\varepsilon}$  an independent and identically distributed (IID) random sample of Bernoulli trials (Montgomery et al., 2001), where each trial is either a “success” or a “failure”. In the perspective of the damage process, the success is associated to the “rupture” event (i.e.  $\varepsilon_p^* < \varepsilon_p(\bar{\varepsilon}, \theta_p)$ ) and the failure to the “no rupture” outcome, i.e.  $\varepsilon_p^* > \varepsilon_p(\bar{\varepsilon}, \theta_p)$ . The probability of success of a single trial is  $P(\bar{\varepsilon}, \theta_p)$  in (44) and the probability density function of the random variable  $n_1(\bar{\varepsilon})$  is the binomial distribution

$$P_{N_1}(n_1(\bar{\varepsilon})) = \binom{N_1}{n_1} P_1^{n_1} \cdot (1 - P_1)^{N_1 - n_1}, \tag{46}$$

with the binomial coefficient expressing the number of possible combinations of sampling  $n_1$  ruptures out of  $N_1$  “trials” in the Bernoulli parlance. The expected value  $\langle n_1(\bar{\varepsilon}) \rangle$  is defined by the weighted average of

$$\langle n_1(\bar{\varepsilon}) \rangle = \sum_{n_1=1}^{N_1} [P_{N_1}(n_1(\bar{\varepsilon})) \cdot n_1], \tag{47}$$

which can be evaluated explicitly from the first derivative of  $\sum_{n_1=1}^{N_1} P_{N_1}(n_1(\bar{\varepsilon})) = 1$  with respect to  $P_1$  in (46), namely

$$\langle n_1(\bar{\varepsilon}) \rangle = P_1 \cdot N_1 = \frac{P_1 \cdot N_0}{3}. \tag{48}$$

The same arguments could be applied to Group 2 once the extent of the active subset  $N_2^* < N_2$  is determined. This is not a trivial task and the value  $N_2^* = N_1/3$  assumed in (37) was estimated from simulations. The damage rate  $\dot{n} = \partial n(\bar{\varepsilon})/\partial \bar{\varepsilon}$  was decomposed into the two contributions  $\dot{n}_1 = \partial n_1(\bar{\varepsilon})/\partial \bar{\varepsilon}$  and  $\dot{n}_{23} = \partial n_{23}(\bar{\varepsilon})/\partial \bar{\varepsilon}$ , with  $n_{23}(\bar{\varepsilon}) = n_2(\bar{\varepsilon}) + n_3(\bar{\varepsilon})$ . A regression analysis of numerical data in the strain range  $\bar{\varepsilon} \in [0.7 \times 10^{-4}]$  provided the estimates  $\dot{n}$ ,  $\dot{n}_1$  and  $\dot{n}_{23}$  reported in the first column of Table 1 (labelled “SIMULATION”) for  $N = \{24, 48, 96, 192\}$ .

Then, according to Table 2, it was noticed that ratios  $\dot{n}_1/\dot{n}_{23}$  cluster around a value close to three for  $N \geq 48$ , suggesting  $\langle n_{23}(\bar{\varepsilon}) \rangle \simeq \langle n_1(\bar{\varepsilon}) \rangle/3$ . Eq. (37) is a consequence.

Table 1  
Prospect of damage rates  $\dot{n}$  and components  $\dot{n}_1$  and  $\dot{n}_{23}$  estimated from simulations data and from the available models for the hardening phase

$N$	Rates	Simulation	Model	Scaling
24	$\dot{n}$	63,892	74,100	58,741
	$\dot{n}_1$	54,187	55,600	/
	$\dot{n}_{23}$	8870	18,500	/
48	$\dot{n}$	277,430	301,867	245,294
	$\dot{n}_1$	209,120	226,400	/
	$\dot{n}_{23}$	66,469	75,467	/
96	$\dot{n}$	1,039,100	1,218,133	1,002,163
	$\dot{n}_1$	792,280	913,600	/
	$\dot{n}_{23}$	253,650	304,533	/
192	$\dot{n}$	4,427,500	4,893,867	4,050,963
	$\dot{n}_1$	3,383,600	3,670,400	/
	$\dot{n}_{23}$	1,078,200	1,223,467	/

Table 2

Dependence of ratio  $\dot{n}_1/\dot{n}_{23}$  estimated from simulations data for different lattice size in the limit of dilute damage

Ratio	24	48	96	192
$\dot{n}_1/\dot{n}_{23}$	6.1	3.15	3.12	3.14

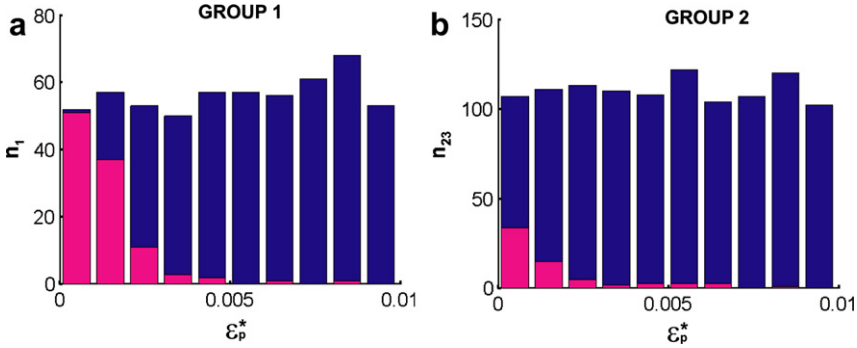


Fig. 13. Histograms of critical strengths  $\epsilon_p^*$  of the  $n_1$  broken bonds in Group 1 (a) and the  $n_{23}$  in Group 2 (b) at the failure overlaid on top of the corresponding histogram of critical strengths quenched in the lattice (blue-dark) for  $N = 24$ . The ordinate axis reports counts and not frequencies/probabilities, obtainable by normalization. (For interpretation of the references in colour in this figure legend, the reader is referred to the web version of this article.)

The latter expression intuitively indicates that about one-third of the lattice domain is invested by a perturbation strong enough to cause diagonal ruptures. Fig. 12b and c show conceptual rupturing schemes for diagonals corresponding to the mean field estimate from (40b) and to the “maximum-field” estimate from Eqs. (42), (37) respectively with reference to the selected quenched distribution of critical strains. The histograms of broken bonds at the failure for  $N = 24$  in Fig. 13 provide numerical confirmation for the assumed damage modes in Fig. 12a and c.

Based on the above arguments, by considering the diagonal ruptures an IID random sample, the probability associated to the  $n_2(\bar{\epsilon})$  and  $n_3(\bar{\epsilon})$  ruptures is

$$P_{N_3}(n_3(\bar{\epsilon})) = P_{N_2}(n_2(\bar{\epsilon})) = \binom{N_2^*/2}{n_2} (P_1)^{n_2} \cdot (1 - P_1)^{N_2^*/2 - n_2} \tag{49}$$

and the expected values  $\langle n_2(\bar{\epsilon}) \rangle$  and  $\langle n_3(\bar{\epsilon}) \rangle$  are computed by permuting  $P_1$  and  $N_1$  with  $P_2/2$  and  $N_2^*/2$  respectively in (46)

$$\langle n_2(\bar{\epsilon}) \rangle = \langle n_3(\bar{\epsilon}) \rangle = \frac{P_2}{2} \cdot \frac{N_2^*}{2} = \frac{P_1 \cdot N_1}{6} = \frac{\langle n_1(\bar{\epsilon}) \rangle}{6}. \tag{50}$$

Simple algebraic manipulations on Eqs. (40a), (42), (48), (50) yield

$$\langle n_1(\bar{\epsilon}) \rangle = \frac{\bar{\epsilon}}{\epsilon_{MAX}} \frac{N_0}{3} = \frac{3}{4} \langle n(\bar{\epsilon}) \rangle, \tag{51a}$$

$$\langle n_2(\bar{\epsilon}) \rangle = \langle n_3(\bar{\epsilon}) \rangle = \frac{\bar{\epsilon}}{\epsilon_{MAX}} \frac{N_0}{18} = \frac{\langle n_1(\bar{\epsilon}) \rangle}{6} = \frac{1}{8} \langle n(\bar{\epsilon}) \rangle, \tag{51b}$$

$$\langle n(\bar{\epsilon}) \rangle = \langle n_1(\bar{\epsilon}) \rangle + \langle n_2(\bar{\epsilon}) \rangle + \langle n_3(\bar{\epsilon}) \rangle = \frac{4}{9} \frac{\bar{\epsilon}}{\epsilon_{MAX}} N_0. \tag{51c}$$

The application of the expectation operator to Eq. (43) leads to the relation

$$\langle \bar{D}(\bar{\varepsilon}) \rangle = \frac{3k}{\bar{K}_0} \left( \frac{\ell_0}{L} \right)^2 \langle n(\bar{\varepsilon}) \rangle, \quad (52)$$

which concludes the derivation and provides the connection between the two macroquantities  $\langle \bar{D}(\bar{\varepsilon}) \rangle$  and  $\langle n(\bar{\varepsilon}) \rangle$ . Expression (52) can be compared against (2) in the form

$$\langle \bar{D}(\bar{\varepsilon}) \rangle = \frac{\langle n(\bar{\varepsilon}) \rangle}{\hat{\alpha}_1 \cdot L^2}, \quad (53a)$$

$$\hat{\alpha}_1 = \frac{\bar{K}_0}{3k\ell_0^2} = 0.34, \quad (53b)$$

where  $\bar{K}_0 = 103$ ,  $k = 100$  and  $\ell_0 = 1$  for our simulations (e.g. Fig. 3d). The value  $\hat{\alpha}_1$  is lower than the estimate  $\alpha_1 = 0.4$  from Krajcinovic and Rinaldi (2005). Consequently, Eq. (53a) would tend to overestimate the damage  $\bar{D}(\bar{\varepsilon})$  from (2) when  $\langle n(\bar{\varepsilon}) \rangle$  and  $n(\bar{\varepsilon})$  were the same, i.e.

$$\frac{\bar{D}(\bar{\varepsilon})}{\langle \bar{D}(\bar{\varepsilon}) \rangle} \cong 0.85. \quad (54)$$

Similarly, the comparison with experimental data in Table 1 computed as  $\bar{D}_{\text{SIM}}/\langle \bar{D} \rangle = \dot{n}/\langle \dot{n} \rangle = \{0.86, 0.92, 0.85, 0.90\}$  yields an error within 10–15%. This seems acceptable, especially because the model can be fine tuned in several ways. For example, a different value for the redistribution factor  $\eta_p$  can be picked or Eq. (42) could be replaced by  $\varepsilon_{(ij)}(\theta = \pm 60^\circ) = \beta \cdot \bar{\varepsilon}$ , where  $\beta$  be a calibration parameter. The empirical position (37) insures that the model has damage rates calibrated against simulations. The numerical estimates  $\langle \dot{n} \rangle$ ,  $\langle \dot{n}_1 \rangle$  and  $\langle \dot{n}_{23} \rangle$  from differentiation of Eqs. (51) are reported in the second column of Table 1 (labeled “MODEL”) and are in fact in good agreement with the simulation data. The estimates  $\dot{n}$  from (3) are reported in the third column too. The similarity between  $\hat{\alpha}_1$  and  $\alpha_1$ , along with consistent damage rates, demonstrates that this statistical model captures the order of magnitude of both  $\bar{D}(\bar{\varepsilon})$  and  $\partial n(\bar{\varepsilon})/\partial \bar{\varepsilon}$  in spite of the numerous assumptions.

### 5.1.1. One-way correlation between diagonal and horizontal ruptures

Although correlation does not imply causality in general, the perturbation of the strain field from the pristine state due to damage clearly introduces a causal relationship between the rupturing processes in the diagonal and horizontal springs. This fact is referred to as “one-way correlation” in the third assumption of our statistical model. A rigorous evaluation of such correlation is pursued here to strengthen the results above. Preliminarily, the concepts of correlation, autocorrelation and  $P$ -value are recalled.

- (1) *Correlation*: “In probability theory and statistics, correlation, also called correlation coefficient, is a numeric measure of the strength of linear relationship between two random variables. In general statistical usage correlation or co-relation refers to the departure of two variables from independence. In this broad sense there are several coefficients, measuring the degree of correlation, adapted to the nature of data”

(Wikipedia). The pair-correlation  $\rho_{xy}$  between two random variables  $X$  and  $Y$  with expected values  $\langle X \rangle$  and  $\langle Y \rangle$  and standard deviations  $\sigma_X$  and  $\sigma_Y$  is one common measure defined as:

$$\rho_{xy} = \frac{\text{cov}(X, Y)}{\sigma_X \sigma_Y} \simeq \frac{\langle XY \rangle - \langle X \rangle \langle Y \rangle}{\sqrt{\langle X^2 \rangle - \langle X \rangle^2} \sqrt{\langle Y^2 \rangle - \langle Y \rangle^2}}. \tag{55}$$

The points  $(X, Y)$  gather closer to the 45° line on a  $X$ – $Y$  plot, called scatter plot, as the correlation increases.

- (2) *Autocorrelation*: “In statistics, the autocorrelation of a discrete time series or a process  $X_t$  is simply the correlation of the process against a time-shifted version of itself. If  $X_t$  is second-order stationary with mean  $\mu$  then this definition is

$$R(k) \simeq \frac{\langle (X_i - \langle X \rangle)(X_{i+k} - \langle X \rangle) \rangle}{\sigma_X^2}, \tag{56}$$

where  $k$  is the time shift being considered (usually referred to as the lag). This function has the attractive property of being in the range  $[-1, 1]$  with 1 indicating perfect correlation (the signals exactly overlap when time shifted by  $k$ ) and  $-1$  indicating perfect anti-correlation” (Wikipedia). Hence, Eq. (56) is a special case of the general Eq. (55).

- (3) *P-value*: The assessment of the significance of the correlation coefficient will rest on the  $P$ -value computed from testing the hypothesis of no correlation based on an asymptotic normal distribution of the correlation  $\rho_{xy}$ . The  $P$ -value is the probability of getting a correlation as large as the observed value by random chance, when the true correlation is zero. If this probability is small, say less than 0.01, then the correlation  $\rho_{xy}$  is significant, i.e. non-zero (Montgomery et al., 2001).

Under the general idea that two interacting links (broken or pristine) are probably close one another and that the perturbation fields are stronger near the ruptures (e.g. Fig. 11), the one-way correlation between the two rupturing processes should reflect into a significant spatial correlation amongst pairs of diagonal and horizontal ruptures. Therefore an attempt is made to identify certain pairs of diagonal and horizontal ruptures with sim-

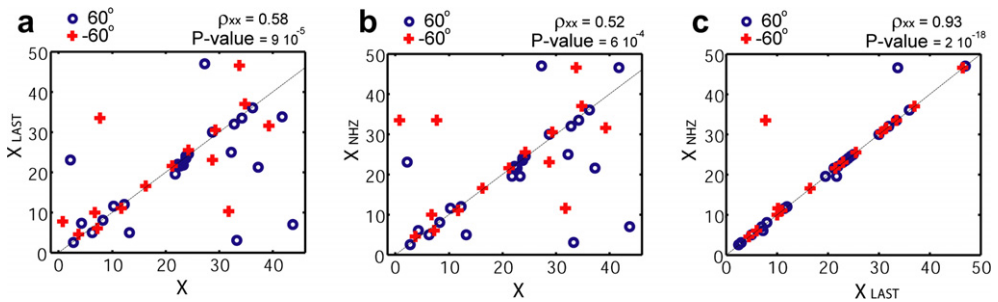


Fig. 14. Scatter plot: (a) between the  $x$ -coordinates  $X$  of a diagonal rupture and the last previous rupture “LAST” (either horizontal or diagonal), (b) between the  $X$  and the nearest horizontal previous rupture “NHZ”, (c) between “LAST” and “NHZ”. Data refer to the first 40 ruptures registered for  $N = 48$ . Circles and crosses corresponds to links with orientations  $60^\circ$  and  $-60^\circ$  respectively. All correlations are significant at a significance level  $\alpha = 0.01$ .

ilar coordinates. For illustrative purposes the analysis will be limited to the first 200 ruptures of the lattice  $N = 48$ , which all occur well within the hardening phase (refer Fig. 3b) and count 160 horizontals and 40 diagonals.

First, we ascertain if there is a relation between the 40 diagonals and the last preceding rupture (of whatever orientation), labeled “LAST”. By taking as  $X$  in Eq. (55) the vector of the  $x$  coordinates of the 40 center points of the diagonal broken links and by letting  $Y = X_{\text{LAST}}$  be the vector of the  $x$  coordinates of the preceding ruptures associated to  $X$ , one can appreciate some correlation from the scatter plot in Fig. 14a. The  $\rho_{xx} = 0.58$  is indeed significant based on the  $P$ -value smaller than 0.01. Similarly, when the  $y$  coordinates are considered, a significant  $\rho_{yy} = 0.44$  is obtained. This observation points out that the 40 diagonals are influenced by previous damage. Although the correlation coefficients are computed by pooling the 40 values, ruptures at  $60^\circ$  and  $-60^\circ$  are marked differently with circles and crosses respectively to show their symmetric statistical behavior.

A second test examines the correlation between the 40 diagonals and the nearest horizontal (preexisting) ruptures, labeled “NHZ”. As above, the scatter plots renders  $(\rho_{xx}, \rho_{yy}) = (0.52, 0.53)$ . Fig. 14b shows just the  $x$  coordinates. This test highlights that the diagonals ruptures tend to form close to horizontal ruptures.

A third test shows the correlation between the datasets LAST and NHZ. The scatter plots in Fig. 14c demonstrate a very high correlation, in the order of 0.9, which suggests that LAST and NHZ might be essentially the same set. If we accept this likely interpretation and follow a transitive logic, these three tests prove that there is a spatial and temporal correlation between each diagonal ruptures and the preceding horizontal rupture. The correlation emerges also from the histograms of “the distance from the previous rupture” (DPR) for Group 1 and Group 2 (not shown). In the former case the histogram resemble a uniform profile typical of non-correlated damage process, while in the latter case the histogram is highly skewed towards lower values.

The lack of autocorrelation within same Group has not been studied systematically via Eq. (56) but through several pair tests based on Eq. (55), which gave meaningful information for our purposes. For example, the scatter plot of  $x$ -coordinates of the 40 diagonal ruptures vs the nearest diagonal ruptures gave a low correlation coefficient  $\rho_{yy} = 0.28$  with a  $P$ -value 0.08, suggesting absence of autocorrelation at the significance level  $\alpha = 0.01$ . Likewise, no evident autocorrelation has been found amongst horizontal links. In summary, this study supports our model but this conclusion is based on pair correlations only. Higher order correlations have been tacitly neglected without checking. For future reference, it should be recognized the possibility that a horizontal rupture (or a cluster or them) might be responsible for more than one diagonal.

## 5.2. Remarks: inputs, hierarchy of sets and anisotropic damage

The rational model presented above demonstrate how the immanent disorder (i.e quenched distribution and orientations of the grain-boundaries) and the lattice kinematics, on both macroscale and microscale, are all compounded into the damage parameter. Eqs. (29), (34), (51) and (52) establish the linkage amongst applied load, spring orientations and distribution of critical strains. Numerical data for  $\eta$  in Fig. 8, for the damage rates in Table 1 and for the microstrains statistics in Fig. 9 provided the input for the statistical models. A coming paper will show that  $\eta$  and  $\varepsilon_{(ij)}^*/\bar{\varepsilon}^*$  are the fundamental random variables providing full input data.

Furthermore, Eq. (53a) renders rationally the  $L^2$  dependence of the damage parameter that was only postulated in (2). It is clear from Eqs. (53) that the damage parameter depends on the ratio  $\ell_0/L$  between the characteristic lengths of the microscale and macroscale. The model contributes to a new perspective of the damage nucleation process by tying the rupturing of diagonal links in Group 2 to the dominant damage process along the most favorably oriented horizontal links. In agreement with Christofer et al., grain boundaries orthogonal to the loading direction have a much higher probability of cracking and deserve the appellation of “primary” or “master”. The “primary” springs break randomly in the lattice domain and are not spatially correlated. The elastic perturbation is very high, already after the first horizontal rupture, and causes the probability of cracking of unfavorably oriented grain boundaries to increase fast. This latter set of grain boundaries can be referred to as “secondary” or “slave” and tends to break near the primary ruptures without interacting with each other. Since the secondary ruptures are perfectly correlated to the primary ruptures but not with each other, the damage nucleation process is globally spatially non-correlated as the primary links. Therefore, the commonly used definition “random non-correlated process” for the damage nucleation is still acceptable by acknowledging that the process is random non-correlated only for the primary set.

The damage evolution and the roles of certain grain boundaries depend on the load configuration in relation to the given microstructure. To illustrate this statement, we take one  $96 \times 96$  triangular lattice containing one horizontal (in  $x$ ) rupture and simulate two separate uniform tensile tests on it, one in the  $x$ -direction and another in the  $y$  directions. The perturbation fields shown in Figs. 15 and 16 demonstrate that the effect of this rupture changes drastically in the two tests. Fig. 15 compares the two perturbation fields affecting the survival horizontals (Group 1) in the two cases. These fields have different shapes and the small strain amplification effect is milder in the second case. Fig. 16 compares the perturbations on the diagonals at  $-60$  (Group 2). Along the  $x$ -axis the results in Fig. 16a are consistent with the large strain effect observed earlier in Fig. 11, while opposite scenario

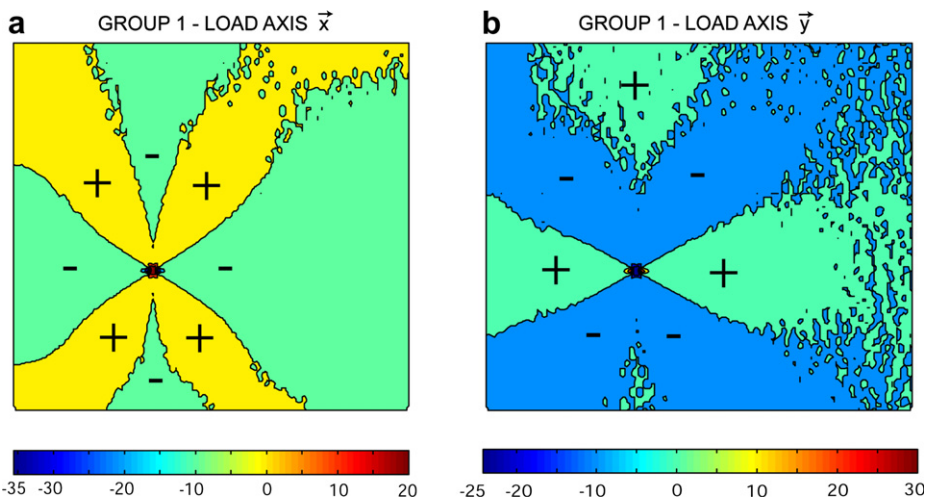


Fig. 15. Percent perturbation fields of survivor horizontal links in a lattice  $N = 96$  with only one horizontal rupture under uniform tension. The load axis is  $\vec{x}$  in (a) and  $\vec{y}$  in (b). The effect is even milder in the latter case.

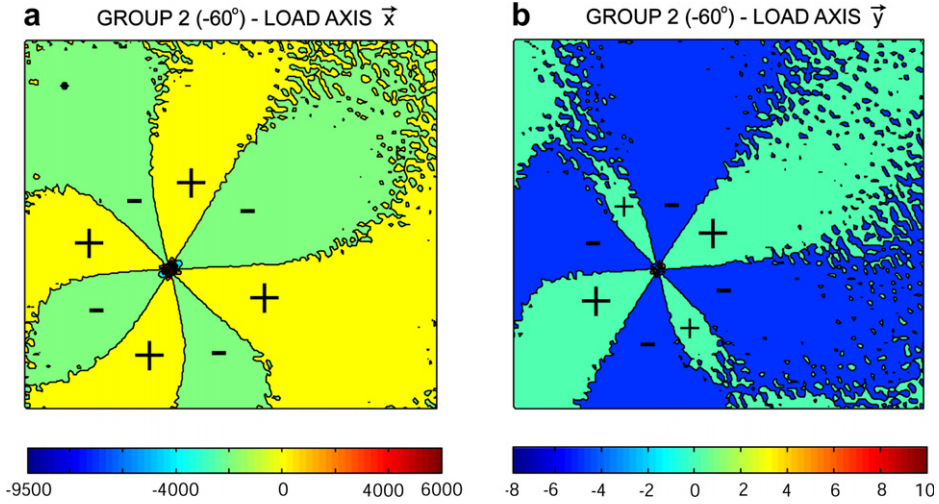


Fig. 16. Percent perturbation fields in survivor diagonal links at  $-60^\circ$  in a lattice of size  $N = 96$  with only one horizontal rupture under uniform tension. The load axis is  $\vec{x}$  in (a) and  $\vec{y}$  in (b). The situations are totally different as evident from the scale ranges.

happens in the test along the  $y$ -axis (Fig. 16b) with a rather negligible tensile perturbation. Although in the latter case the chosen horizontal spring associated to a compressed high angle grain boundary would not be the first to break, such microcrack is plausible because it could still originate in the microstructure during previous loading, manufacturing and environment (e.g. load reversal, wear, plasticity, fatigue, corrosion, cooling, etc.). Clearly, the horizontal springs are not a “primary” group if  $y$ -axis is the loading axis and do not trigger any damage acceleration in diagonal links. Consequently, the damage evolution will develop according to two different patterns, as well as the elastic anisotropy. Even a material isotropic in the pristine state like our triangular lattice acquire during damage nucleation a specific anisotropy reflecting the faster depletion of the primary links for the given loading scheme.

The dependence of the “hierarchy of sets” on the loading conditions is of great importance and must reflect in the constitutive relations, such as Eqs. (1) and (2) for the tensile test inhere. In the ambit of multiaxial loading, this is a formidable task requiring a lengthy characterization of the whole damage tensor case by case. Evidently, statistical damage mechanics and rational models, like these ones for the lattice, can be valuable tools to investigate the mutual interactions amongst microcracks with different inclinations in well characterized microstructures. This approach might eventually lead to a consistent theoretical framework for damage tensor, damage surfaces and flow rules analogously to the theory of plasticity. In this direction, a systematic study of the damage process in lattices subject to multiaxial loading is being conducted. For modeling anisotropic damage in disordered microstructure containing “ $p$ ” orientations, the vector  $\mathbf{n}(\bar{\varepsilon}) = [n_1(\bar{\varepsilon}), n_2(\bar{\varepsilon}), \dots, n_p(\bar{\varepsilon})]$  for all  $p$  components must be monitored rather than the aggregate scalar  $n(\bar{\varepsilon})$ . In the continuum limit, this vector is replaced by the function  $\mathbf{n}(\bar{\varepsilon}, \theta_p)$  defined on a continuous spectrum of orientations in the interval  $\theta_p = [0, \pi]$ .

As a final note, if a full mean-field model were developed alternatively by endorsing both Eq. (40), such model would miss  $\bar{D}(\bar{\varepsilon})$  as well as the damage rates, i.e. the individual damage evolution for each Group. The interested reader can repeat the derivation and verify that the mean-field estimates would be

$$\hat{\alpha}_1 = \frac{\bar{K}_0(1 - \nu)}{2k\ell_0^2} \left[ 1 + 2 \left( \frac{1 - 3\nu}{4} \right)^3 \right]^{-1} = 0.36, \tag{57a}$$

$$\langle n_1(\bar{\varepsilon}) \rangle = \frac{\bar{\varepsilon}}{\varepsilon^{\text{MAX}}} \frac{N_0}{3} = \frac{2}{3 - 3\nu} \langle n(\bar{\varepsilon}) \rangle, \tag{57b}$$

$$\langle n_2(\bar{\varepsilon}) \rangle = \langle n_3(\bar{\varepsilon}) \rangle = \frac{1 - 3\nu}{4} \frac{\bar{\varepsilon}}{\varepsilon^{\text{MAX}}} \frac{N_0}{3} = \frac{1 - 3\nu}{4} \langle n_1(\bar{\varepsilon}) \rangle = \frac{1 - 3\nu}{2(3 - 3\nu)} \langle n(\bar{\varepsilon}) \rangle. \tag{57c}$$

The alternative mean-field approach is noteworthy because it constitutes the discrete counter part of continuum micromechanical models built under similar assumptions, e.g. the RVE from dilute concentration models and other references in the introduction. Hence, these findings can serve also to elaborate more refined RVE of continuum micro-mechanics by introducing conditional probability of ruptures depending on loading and microstructure as done in this paper.

## 6. Conclusions

The main conclusions of this discourse are highlighted below.

- The macroscopic loss of strain energy due to damage can be broken into three contributions with clear meaning, both for a single microcrack and for an avalanche. The perturbation field induced in the lattice by damage formation is proved to maximize the energy dissipation. Such analysis culminate with the introduction of the redistribution parameter  $\eta$  necessary for the rational model.
- The damage parameter  $\bar{D}$  can be computed from the connection between the macroscopic loss of stiffness and local load redistribution capability of the lattice. The rational closed form model derived from statistical reasoning using simulations data as inputs is an example of a rigorous bottom-up strategy for the computation of  $\bar{D}$  in the hardening phase from the study of the microfield of strains. Although the paper is limited to random lattices with perfect geometry, the results support and clarify the definitions recalled in Section 2 from earlier work. In general, random morphology (grain boundary orientations) and mechanical properties of a disordered microstructure are finely mixed with the macroscale kinematics through  $\bar{D}$  as in Eq. (34). The approach is appealing for the good agreement with the numerical data, not only in terms of  $\bar{D}$  but of damage rates.
- Numerical simulations are necessary to estimate microscale-related data (e.g.  $\eta$ ,  $\Delta U_3^{\text{TOT}}$ ,  $\varepsilon_{(ij)}^*/\bar{\varepsilon}^*$ ,  $n_i(\bar{\varepsilon})$ , etc.) that cannot normally be extracted from real experiments.
- This study underscores a hierarchy of spring sets, which play different roles in the rupturing process depending on their orientation with respect to the applied load. Through an example, it is also shown that different loading schemes generate totally different perturbation fields in the microstructure, determining totally different damage evolutions. Knowledge of the scalar  $n(\bar{\varepsilon})$  is not sufficient and more complex parameters (e.g. the vector  $\mathbf{n}(\bar{\varepsilon}, \theta_p)$ ) are required by a modeling perspective.

The identification of a functional hierarchy of subgroups of grain boundaries in a microstructure (related to morphological parameters, such as orientation but not only), the comprehension of their roles in all the stages of a damage process, the understanding that nucleation is not a random non-correlated process and the sane criticism towards the “isotropic damage” hypothesis are all elements that set the stage for the application of discrete statistical models to the study of anisotropic damage from multiaxial loading. Work is being carried out to complete the rational treatment of the lattice model but in the future it would be necessary to apply this framework to models employing solid elements instead of springs. In the logic of a modular approach, discrete models could be interfaced with a continuum models on the macroscale analogously to the RVE.

### Acknowledgements

This research is sponsored by the Mathematical, Information and Computational Science Division, Office of advanced Scientific Computing Research, US Department of Energy under contract # DE-AC05-00OR22725 with UT-Battelle, LLC. Antonio Rinaldi expresses his gratitude to Prof. Dusan Krajcinovic for his inspiring mentorship over the years.

### References

- Audoin, B., Baste, S., 1994. Ultrasonic evaluation of stiffness tensor changes and associated anisotropic damage in a ceramic matrix composite. *J. Appl. Mech.* 61, 309–316.
- Betten, J., 1983. Damage tensors in continuum mechanics. *J. Mech. Theor. Appl.* 2, 13–32.
- Bonora, N., Gentile, D., Pironi, A., Newaz, G., 2005. Ductile damage evolution under triaxial state of stress: theory and experiments. *Int. J. Plasticity* 21, 981–1007.
- Brüning, M., 2004. Eshelby stress tensor in large strain anisotropic damage mechanics. *Int. J. Mech. Sci.* 46, 1763–1782.
- Budiansky, B., O’Connell, R.J., 1976. Elastic moduli of a cracked solid. *Int. J. Solids Struct.* 12, 81–97.
- Cannmo, P., Runesson, K., Ristinmaa, M., 1995. Modelling of plasticity and damage in a polycrystalline microstructure. *Int. J. Plasticity* 11 (8), 949–970.
- Chaboche, J.L., 1988a. Continuum damage mechanics: Part I—General concepts. *J. Appl. Mech.* 55, 59–64.
- Chaboche, J.L., 1988b. Continuum damage mechanics: Part II—Damage growth, crack initiation, and crack growth. *J. Appl. Mech.* 55, 65–72.
- Chow, C.L., Wang, J., 1987. An anisotropic theory of continuum damage mechanics for ductile fracture. *Eng. Frac. Mech.* 27, 547–558.
- Christopher, A., Mukul, K., Wayne, K.E., 2003. Analysis of grain boundary networks and their evolution during grain boundary engineering. *Acta Mater.* 51, 687–700.
- Cordebois, J.P., Sidorff, F. 1979. Damage induced anisotropy. *Colloque Euromech*, 115, Villard de Lans.
- Curtin, W.A., Scher, H., 1990. Brittle fracture in disordered materials. *J. Mater. Res.* 5 (3), 535–553.
- Delaplace, A., Pijaudier-Cabot, G., Roux, S., 1996. Progressive damage in discrete models and consequences on continuum modelling. *J. Mech. Phys. Solids* 44 (1), 99–136.
- Gurtin, M.E., 1975. In: Truesdell, C. (Ed.), *Handbook der Physics*, vol. IV.
- Hansen, N.R., Schreyer, H.L., 1994. A thermodynamically consistent framework for theories of elastoplasticity coupled with damage. *Int. J. Solids Struct.* 31 (3), 359–389.
- Hansen, A., Roux, S., Herrmann, H.J., 1989. Rupture of central-force lattices. *J. Phys. France* 50, 733–744.
- Hayhurst, D.R., 1972. Creep rupture under multiaxial state of stress. *J. Mech. Phys. Solids* 20, 381–392.
- Hegemier, G.A., Read, R.H., 1985. On deformation and failure of brittle solids: some outstanding issues. *Mech. Mater.* 4, 215–259.
- Horii, H., Nemat-Nasser, S., 1983. Overall moduli of solids with micro-cracks: load-induced anisotropy. *J. Mech. Phys. Solids* s31, 155–171.

- Hrennikoff, A., 1941. Solution of problems of elasticity by the framework method. *J. Appl. Mech. (Trans. ASME)* 8, A169–A175.
- Jagota, A., Bennison, S.J., 1995. Element breaking rules in computational models for brittle fracture. *Modell. Simul. Mater. Sci. Eng.* 3, 485–501.
- Ju, J.W., 1990. Isotropic and anisotropic damage variables in continuum damage mechanics. *J. Eng. Mech.* 116, 2764–2770.
- Krajcinovic, D., 1983. Constitutive equations for damaging materials. *J. Appl. Mech.* 50, 355–360.
- Krajcinovic, D., 1996. *Damage Mechanics*. North-Holland, Amsterdam, The Netherlands.
- Krajcinovic, D., Basista, M., 1991. Rupture of central-force lattices revisited. *J. Phys. I* 1, 225–241.
- Krajcinovic, D., Fonseka, G.U., 1981a. The continuous damage theory of brittle materials. Part 1: General theory. *J. Appl. Mech.* 48, 809–815.
- Krajcinovic, D., Fonseka, G.U., 1981b. The continuous damage theory of brittle materials. Part 2: Uniaxial and plane response modes. *J. Appl. Mech.* 48, 816–824.
- Krajcinovic, D., Rinaldi, A., 2005. Statistical damage mechanics – 1. Theory. *J. Appl. Mech. (72)*, 76–85.
- Krajcinovic, D., Vujosevic, M., 1998. Strain localization – short to long correlation length transition. *Int. J. Solids Struct.* 35 (31–32), 4147–4166.
- Lemaitre, J., 1985a. A continuous damage mechanics model for ductile fracture. *J. Eng. Mater. Tech.* 107, 83–89.
- Lemaitre, J., 1985b. Coupled elasto-plasticity and damage constitutive equations. *Comput. Methods Appl. Mech. Eng.* 51, 31–49.
- Lemaitre, J., 1996. *A Course on Damage Mechanics*, second ed. Springer, Berlin.
- Litewka, A., Debinski, J., 2003. Load-induced oriented damage and anisotropy of rock-like materials. *Int. J. Plasticity* 19, 2171–2191.
- Lubarda, V.A., Krajcinovic, D., 1995. Some fundamental issues in rate theory of damage-elastoplasticity. *Int. J. Plasticity* 11, 763–797.
- Mariano, P.M., Stazi, F.L., 2001. Strain localization in elastic microcracked bodies. *Comput. Methods Appl. Mech. Eng.* 190, 5657–5677.
- Mastilovic, S., Krajcinovic, D., 1999. Statistical models of brittle deformation: Part II: Computer simulations. *Int. J. Plasticity* 15, 427–456.
- Monette, L., Anderson, M.P., 1994. Elastic and fracture properties of the two-dimensional triangular and square lattices. *Modell. Simul. Mater. Sci. Eng.* 2, 53–66.
- Montgomery, D.C., Peck, E.A., Vining, G.G., 2001. *Introduction to Linear Regression Analysis*. Wiley.
- Murakami, S., 1988. Mechanical modeling of material damage. *J. Appl. Mech.* 55, 280–286.
- Pierard, O., Doghri, I., 2006. An enhanced affine formulation and the corresponding numerical algorithms for the mean-field homogenization of elasto-viscoplastic composites. *Int. J. Plasticity* 22, 131–157.
- Rinaldi, A., Mastilovic, S., Krajcinovic, D., 2006a. Statistical damage mechanics—2. Constitutive relations. *J. Theor. Appl. Mech.* 44, 3.
- Rinaldi, A., Peralta, P., Krajcinovic, D., Lai, Y.C., 2006b. Prediction of fatigue properties with discrete damage mechanics. *Int. J. Fatigue* 28, 1069–1080.
- Rinaldi, A., Mastilovic, S., Krajcinovic, D., 2007. Extreme value theory and statistical damage mechanics. *Int. J. Damage Mech.* 16, 1.
- Saczuk, J., Hackl, K., Stumpf, H., 2003. Rate theory of nonlocal gradient damage-gradient viscoelasticity. *Int. J. Plasticity* 19 (5), 675–706.
- Sahimi, M., 2000. *Heterogeneous Material II*. Springer, New York, USA.
- Simo, J.C., Ju, J.W., 1987. Strain- and stress-based continuum damage models—I. Formulation. *Int. J. Solids Struct.* 23, 821–840.
- Tvergaard, V., 1990. Material failure by void growth to coalescence. *Adv. Appl. Mech.* 27, 83–151.
- Van Mier, J.G.M., Vliet, M.R.A., Wang, T.K., 2002. Fracture mechanisms in particle composites: statistical aspects in lattice type analysis. *Mech. Mater.* 34, 705–724.
- Voyiadjis, G.Z., Kattan, P.I., 1999. *Advances in Damage Mechanics: Metals and Metal Matrix Composites*. Elsevier, Amsterdam.
- Voyiadjis, G.Z., Abu Al-Ruba, R.K., Palazotto, A.N., 2004. Thermodynamic framework for coupling of non-local viscoplasticity and non-local anisotropic viscodamage for dynamic localization problems using gradient theory. *Int. J. Plasticity* 20, 981–1038.
- Wikipedia: <http://en.wikipedia.org>.